Eindhoven University of Technology

MASTER

Laser Pulse Stretching for Spontaneous Raman Spectroscopy of Plasma Assisted Combustion

Gijbels, T.G.

Award date:
2020

EINDHOVEN
UNIVERSITY OF
TECHNOLOGY

Department of Applied Physics

Laser Pulse Stretching for Spontaneous Raman Spectroscopy of Plasma Assisted Combustion

Timothy Gareth Gijbels
0814031 - EPG

Daily Supervisor
R.B. Patel, MSc

Examination Committee

dr.ir.	S. Nijdam	(chair)
dr.	N.J. Dam	
dr.	R.A.H. Engeln	
dr.ir.	J.C.H. Zeegers	
	R.B. Patel,	MSc

Eindhoven, The Netherlands
16 October 2020

Abstract

Plasma assisted combustion is a promising way of enhancing combustion efficiency. Researching this, Ravi Patel has developed a nanosecond pulsed dielectric-barrier discharge used for combustion ignition. This study has supported Ravi's research by introducing a high power Nd:YAG laser to replace a weaker laser and enhance the signal of rovibrational spontaneous Raman spectroscopy. Focusing this 10 Hz 9 ns 700 mJ Nd:YAG laser will induce optical breakdown. To prevent this, a laser pulse stretcher was build to spread out the energy deposition of a laser pulse from 9 ns to 40 ns. The energy transmission of this system was 54% resulting in pulse powers of $P_{pulse,new} = (9.5 \pm 0.1)\,\mathrm{MW}$. This leads to a higher signal to noise ratio compared to the weaker laser ($P_{pulse,old} = 0.12\,\mathrm{MW}$), but not necessarily to faster measurements because of the higher frequency of the previous laser (3 kHz). The power of the new pulse stretched laser was not high enough for feasible single shot rovibrational temperature measurements. Therefore, multiple shots were used to measure the Raman spectrum of N_2 in the post-discharge of a non-equilibrium plasma in air. The results showed that the new laser does indeed allow for higher vibrational bands to become visible. However, the absolute values of the rovibrational temperatures were almost an order of magnitude lower than literature values. This was mostly attributed to a lower plasma pulse energy, the use of a dielectric, and potential misalignments of the laser with the plasma.

Acknowledgements

Hello,

You are about to read my Master Thesis: the culmination of my studies at Eindhoven University of Technology. The work presented here bears my name, but would not have existed without the following people.

Ravi Patel, thank you for your continuous positive guidance throughout the entire project, and for answering every single question I had. I cannot overstate how important both of those things were for the success of my thesis. Sander Nijdam and Nico Dam, for your weekly insightful feedback, suggestions, and jokes. Special shout-out to all three of you for your instant replies to emails outside of meeting-times: such committed involvement in my project was never something I took for granted.

Additionally I would like to thank everyone else who helped support this project. Jeroen, Rick, Yunus: for your direct participation. The Gemini lab technicians: in particular Martin. And not least of all: every single one of my friends, family, and my girlfriend. You have all genuinely helped me through university in your own unspoken ways.

Most importantly, I would like to express my sincere gratitude to my parents (Ricardo, Marion), and my brother (Joey) who's unfailing support of my education extends further back than any report or lecture hall.

Stay awesome,
Timothy

> "It is not our part to master all the tides of the world,
> but to do what is in us for the succor of those years wherein we are set"
>
> *J.R.R. Tolkien*
> *The Return of the King*

Contents

Nomenclature

Physical Constants

c	Speed of light
h	Planck constant
k	Boltzmann constant

List of Abbreviations

AC	Alternating current
BS	Beamsplitter
CCD	Charge-coupled device
DBD	Dielectric-barrier discharge
DC	Direct current
FWHM	Full width at half maximum
HV	High voltage
HWP	Half waveplate
ICCD	Intensified charge-coupled device
Nd:YAG	Neodymium-doped yttrium aluminum garnet
Nd:YLF	Neodymium-doped yttrium lithium fluoride
PAC	Plasma assisted combustion
PLIF	Planar laser-induced fluorescence
SLPM	Standard litre per minute
SNR	Signal to noise ratio

SSR	Sum of squared residuals

Chemical Species

CH_4	Methane
CO_2	Carbon dioxide
e^+	Electron
H_2O	Dihydrogen monoxide (water)
H	hydrogen
${N_2}^+$	Nitrogen ion
N_2	Nitrogen
NOx	Nitrogen oxides
O_2	Diatomic oxygen
O_3	Ozone
O	Oxygen

List of Symbols

(A/F)	Actual air-fuel ratio
$(A/F)_{stoic}$	Stoichiometric air-fuel ratio
$\frac{d\sigma}{d\Omega}$	Differential crosssection of a Raman transition
γ	Secondary electron emission coefficient
λ	Wavelength
ϕ	Equivalence ratio
Θ	Angle
A, B	Species dependent constants
d	Gap distance between electrodes
d_t	Temporal pulse width of a laser
E	Energy
$E_{electronic}$	Electronic energy

E_{ext}	External electric field
E_{im}	Statistical energy of quantum state m and species i
$E_{molecular}$	Molecular energy
$E_{nuclearspin}$	Angular moment of individual particle
$E_{rotational}$	Rotational energy
E_{vib}	Vibrational energy
f	Focal length
g_{im}	Statistical weight of quantum state m and species i
I	Current
I	Intensity
J	Rotational energy level
L	Optical cavity path length
m_{air}	Mass of air
m_{fuel}	Mass of fuel
N_i	Concentration of species i
P	Power
p	Pressure
R_{bs}	Beamsplitter reflectivity
R_m	Mirror reflectivity
T	Temperature
T	Transmission
t	Time
T_{rot}	Rotational temperature
T_{vib}	Vibrational temperature
V	Voltage
v	Vibrational energy level
V_{br}	Breakdown voltage
Z_i	Partition function of species i

CHAPTER 1

Introduction

1.1 Motivation

Combustion is an important part of our everyday lives, with applications ranging from commercial vehicles to energy plants to household boilers. Approximately 80% of energy conversion in the world today is due to combustion [1, 2]. However, in recent years concerns have been raised in regards to climate change due to the excessive emission of carbon dioxides (CO_2) [3, 4], and the negative effects of nitrogen oxide (NO_x) emissions on both human health and nature [5, 6, 7]. As such we need to look for better options for a more sustainable future.

Alternative energy sources such as solar and wind power, in combination with a world-wide switch to electrical-based engines holds great promise. Sadly, the logistics of such a drastic change in infrastructure will take decades [8]. In addition to this, there is a scaling problem with electric engines in, for example, the aviation industry due to the relatively low energy density of such engines [9, 10]. As a result combustion will continue to hold a prominent place within the energy-industry in the foreseeable future. Consequently, developing methods to more efficiently burn fuels will have a lasting impact both in the near-future and beyond.

Plasma (ionised gas) affects the combustion process through thermal, kinetic, and transport mechanisms. Due to this wide range of effects, plasma assisted combustion (PAC) has considerable potential in combating the energy crisis. Especially since the turn of the millennium research on PAC has increased in intensity [11, 12].

Recently Elkholy [13] developed a microplasma reactor applied to a flat flame burner. Analysis of this reactor resulted in the conclusion that the plasma mainly contributed in a thermal pathway. To get a more fundamental idea of the effect of plasma on combustion, a new setup has been designed by Ravi Patel, where the plasma and flame are combined in the same probe volume. This symbiotic configuration allows for the investigation of plasma assisted ignition of combustion.

Raman measurements on both setups pointed out that the background noise during plasma measurements was too big to discern a significant signal. As such it was decided to introduce a more powerful Nd:YAG laser to the experiments. There have been reports of such lasers being used for single shot temperature measurements [14, 15].

This thesis presents the efforts of applying a temporal pulse stretcher to this high power Nd:YAG laser to make it suitable for spontaneous Raman spectroscopy. This has subsequently been applied to measure temperatures in the post-discharge of plasma streamers that have been observed to ignite a flame.

1.2 Outline

A theoretical background of the relevant topics will be laid out in chapter 2. Some basics in plasma physics and combustion science will be recounted, and recent advances in plasma assisted combustion are also presented. This chapter will wrap up with an overview of some of the physics behind spontaneous Raman spectroscopy.

A high power Nd:YAG laser was introduced to the setup for Raman spectroscopy measurements. However, the application of such high power equipment for spectroscopic means is not trivial, seeing as focusing it will induce an optical breakdown. Chapter 3 will cover the laser pulse stretcher that was build to mould this laser into a viable diagnostics tool.

Chapter 4 will treat the rest of the experimental setup used for plasma assisted combustion measurements. The vacuum chamber, the nanosecond pulsed dielectric-barrier discharge, the data acquisition, and data analysis tools will be introduced.

Some trial rovibrational spontaneous Raman spectroscopy measurements were performed to test the waters with the pulse stretched laser. Subsequently, the post-discharge temperature of nitrogen was measured at 500 mbar and 100 mbar. The discussion of the experimental results will be addressed in chapter 5.

Last but not least, all of the conclusions and future recommendations will be summarised in chapter 6.

This page is intentionally left blank

CHAPTER 2

Theoretical Background

This chapter is meant to give the reader some basic understanding off the theory on the issues described in this thesis.

2.1 Plasma

Plasma, sometimes referred to as the fourth state of matter, is a cloud of ionized gas. Its main components are positively charged ions, negatively charged electrons, free radicals, and other excited species [13]. Unless stated otherwise, most of the theory presented in this section is based on "*Principles of Plasma Discharges and Materials Processing*" by M.A. Lieberman and A.J. Lichtenberg [16].

2.1.1 Breakdown

The simplest example of how a molecule is ionized is through the process of electron ionization, where a highly energized free electron collides with a gas molecule, releasing an additional electron from the molecule's shell. For example, in the case of nitrogen such a collision can be expressed as

$$\mathrm{e}^- + \mathrm{N}_2 \longrightarrow 2\,\mathrm{e}^- + {\mathrm{N}_2}^+, \tag{2.1}$$

with e^- the negatively charged electron, N_2 the neutral nitrogen molecule, and ${\mathrm{N}_2}^+$ its ion reaction product.

The initial highly energized electron (called the seed electron) can gain its energy through a number of ways. The most common way in man made plasmas is with the help of an external electric field. This field will supply the seed electron with enough energy to start ionizing the molecules, and it will subsequently also accelerate the newly created electron from equation 2.1. This new electron can go on to ionize another molecule, leading to an ever increasing electron avalanche, commonly referred to as a Townsend discharge (Fig. 2.1). The free electrons will move into the direction of the positively charged anode, whereas the newly created ions will move towards the negative cathode, separating the two charged species.

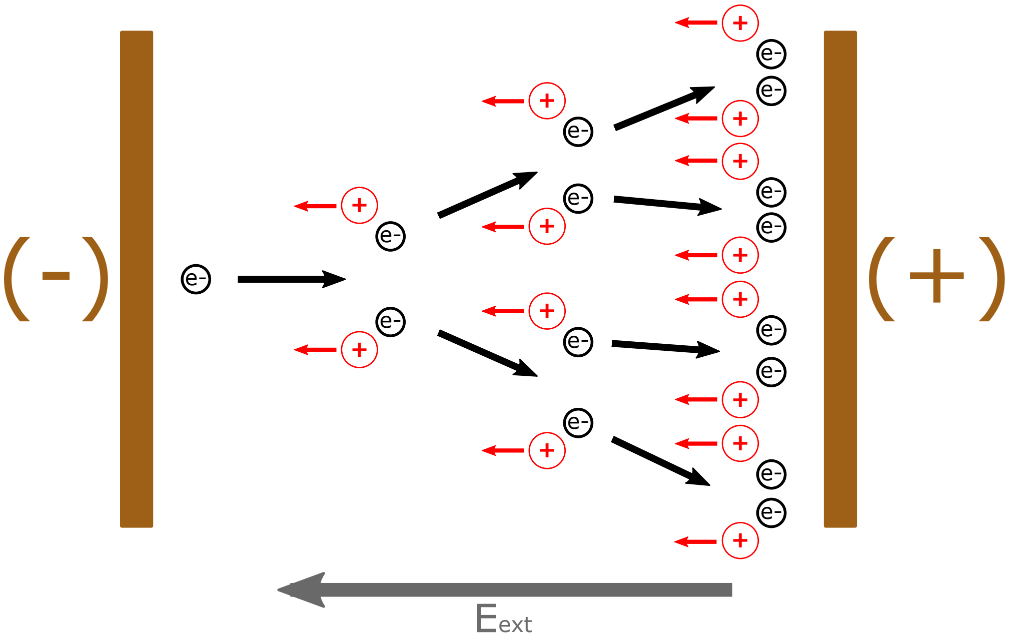

Figure 2.1. *Sketch of the principle mechanism behind a Townsend avalanche. Free electrons gain energy from an external electric field (E_{ext}), and subsequently collide with gas molecules to produce ions and more electrons.*

A full electrical breakdown such as this only happens when the external electric field is strong enough to accelerate the free electrons to the appropriate level. The critical breakdown voltage depends on the gas and is often expressed in the form of Paschen's law (Fig. 2.2) as

$$V_{br}(pd) = \frac{Bpd}{\ln(Apd) - \ln(\ln(1+\frac{1}{\gamma}))}, \tag{2.2}$$

with p the pressure, d the gap distance between electrodes, γ the secondary electron emission coefficient (secondary electrons produced by ions hitting the cathode), and A and B constants dependent on the gas species.

Plasmas are often categorized by means of their temperatures [13]. High temperature equilibrium plasmas are plasmas where the gas, ion, and electron temperatures are all equal ranging from $10^6 - 10^8$ K. Low temperature quasi-equilibrium (thermal) plasmas are plasmas where all species are in thermal equilibrium, but at temperatures smaller than 2×10^4 K.

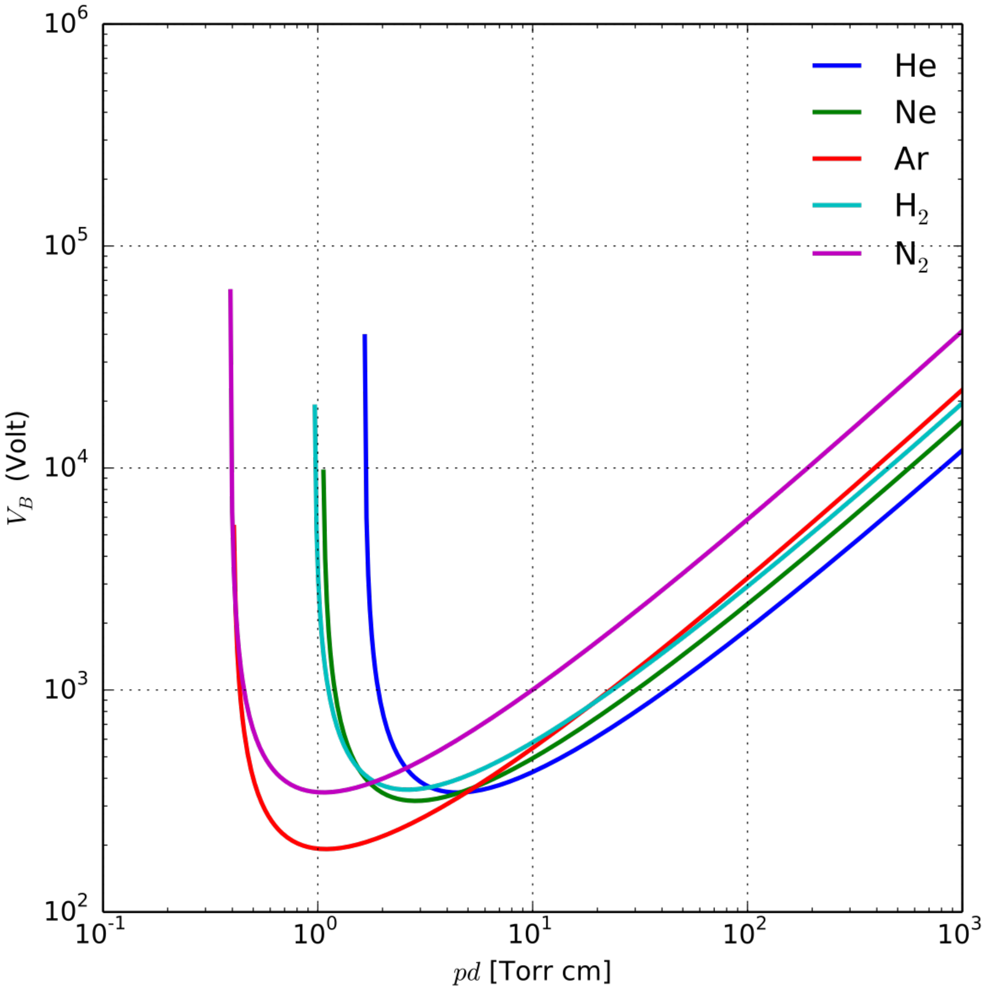

Figure 2.2. *The Paschen curves of a collection of gasses, detailing the critical breakdown voltage [17].*

Lastly there are the low temperature non-equilibrium (non-thermal) plasmas where the electron temperature is in the order of 10^4 K, whereas the heavy ions and gas molecules are around room temperature (or slightly higher, up to 10^3 K).

For the purposes of this study we are mostly interested in the last group of low temperature non-equilibrium plasmas. These are electrically driven discharges which are generally more energy efficient to make (input energy goes into electrons instead of gas), while still producing all the radical species that give plasmas their wide range of industrial applications [18].

2.1.2 Dielectric-Barrier Discharge

As mentioned in section 2.1.1 non-equilibrium plasmas are electrically driven. When the electric field is produced by two separated metal electrodes we speak of a capacitively coupled plasma. A special configuration of the capacitively coupled plasma is the dielectric-barrier discharge (DBD). In this configuration a dielectric material is placed between the electrodes. The main advantage of using a dielectric-barrier discharge is the fact that it will prevent a plasma streamer from transitioning to a thermal arc discharge by limiting the current [19]. All this happens while maintaining a high electric field, which subsequently allows for a non-equilibrium plasma at atmospheric conditions.

An additional benefit of a DBD is that the dielectric will act as an insulator protecting the electrodes from erosion [20].

When an external electric field creates a plasma, the charged species will be separated with the electrons moving towards the positive anode and the ions towards the negative cathode (Fig. 2.1). This separation leads to an induced electric field inside the plasma, in opposite direction of the external electric field. When a dielectric barrier is inserted in front of an electrode, the charged species that were originally moving towards said electrode will instead cluster on top of the dielectric leading to a slow buildup of this internal electric field. At some point the total electric field will be reduced to below the critical value, wiping out the plasma. To prevent this from happening a DBD has to be operated with an alternating current (AC), or a pulsed direct current (DC).

The need for specific voltage sources is not necessarily a downside. Nanosecond pulsed discharges have been found to reduce the consumed power while still resulting in the same electron density as their DC counterparts [21]. This happens when the time between pulses is shorter than the recombination rate of the active species, as such still leading to a high electron density [13]. Additionally, because of the pause in between pulses, less energy goes into heating the gas resulting in a more energy efficient system.

2.2 Combustion

Combustion can be defined as a rapid exothermic chemical reaction, requiring a fuel and an oxidant, resulting in oxidation products, heat, and (possibly) light. Combustion is generally categorised in two modes: flame and nonflame. Before going forward, it is worth noting that (unless stated otherwise) most of the theory presented in this section is based on "*An Introduction to Combustion: Concepts and Applications*" by S.R. Turns [22].

The flameless mode is a form of combustion where the fuel is heat up to above the ignition temperature before getting into contact with the oxidant [23, 24]. It is called flameless because it does not need the flame temperature to sustain combustion. High temperature flameless combustion is a relatively new field, with the first commercial burners appearing in 1991 [25]. A prominent advantage of nonflame combustion is, amongst other things, a decrease in NO_x emissions.

The flamemode of combustion is the more classical image people have of combustion, where the flame itself is actively involved in the process. Flames are further categorised in two classes: premixed flames and nonpremixed (diffusion) flames. These classes refer to the method by which the fuel and oxidant are brought together before ignition. With premixed flames the reactants are mixed together before being directed towards the location of ignition (such as in a Bunsen burner). With nonpremixed flames the reactants meet at the flame front (such as in an everyday candle).

Combustion is a complex process, and the science behind it could actually be seen as a combination of three fields of study: chemistry, thermodynamics, and fluid mechanics. It is nearly impossible to limit yourself to only one of these fields when explaining combustion, without at least putting clear boundary conditions on the others. Therefore, the following subsections will briefly explain some of the basics that are relevant to our study.

2.2.1 Chemistry

Some elementary chemical aspects of combustion can be described with the help of atom balances. For example, the burning of methane (CH_4) in air can be expressed as

$$\mathrm{CH_4} + 2\,\mathrm{O_2} + 7.52\,\mathrm{N_2} \longrightarrow \mathrm{CO_2} + 2\,\mathrm{H_2O} + 7.52\,\mathrm{N_2}, \tag{2.3}$$

where the composition of air is simplified as being 21% oxygen (O_2) and 79% nitrogen (N_2).

This ideal composition of fuel and air is called the stoichiometric air-fuel ratio, representing a complete combustion process (meaning that there is no fuel left after the interaction with the oxidizer). The stoichiometric air-fuel ratio is

$$(A/F)_{stoic} = (m_{air}/m_{fuel})_{stoic}, \tag{2.4}$$

with m_{air} and m_{fuel} the mass of the air and fuel as found in a complete combustion process, such as in equation 2.3.

It's worth noting that even if one has the perfect stoichiometric quantity of reactants, a perfectly complete combustion process rarely occurs. The process of turning CH_4 into CO_2 is a bit more convoluted than equation 2.3 would suggest. In reality the process is better represented in Fig. 2.3, where it shows the multitude of pathways that can lead to either complete combustion (producing CO_2) or incomplete combustion (producing longer and longer carbon chains, soot).

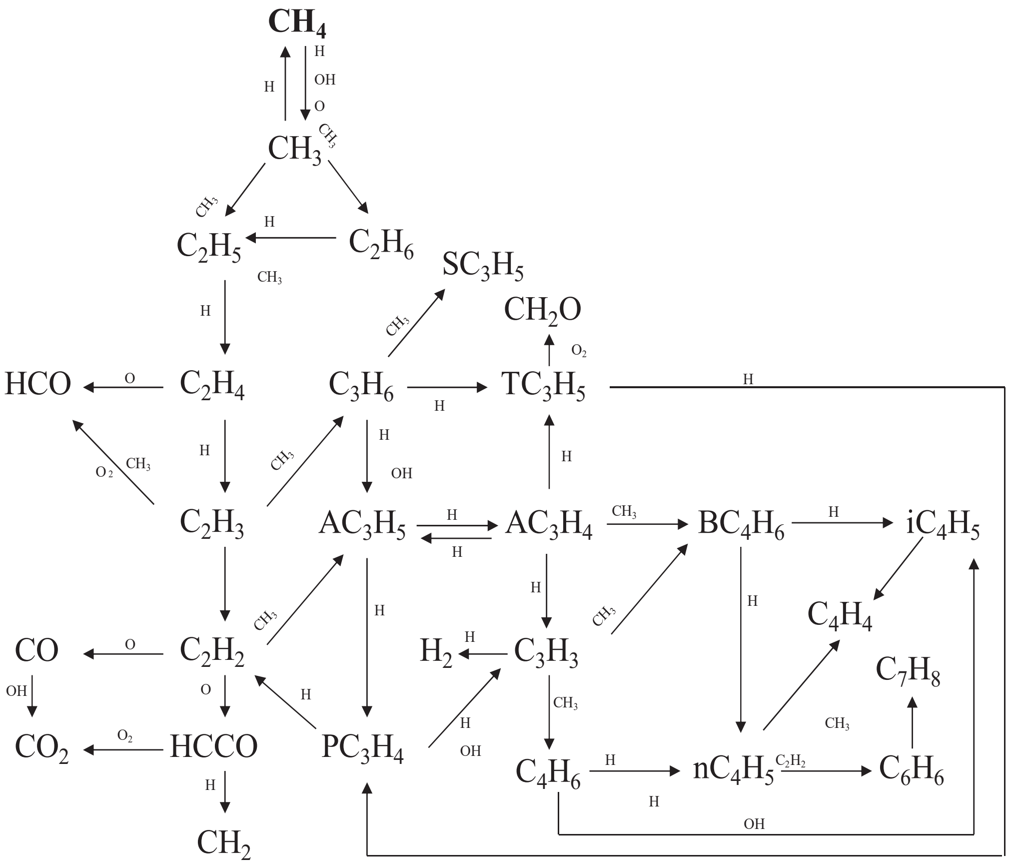

Figure 2.3. *The reaction pathways of methane [26]. There are numerous roads leading to* CO_2*, and so to complete combustion. However, there is also the possibility of other reactions occuring leading to longer and longer carbon chains, eventually producing soot.*

If a reaction has more oxidizer present than the stoichiometric quantity, then the mixture is called lean. If the fuel is over-represented, the mixture is called rich. A commonly used unit to determine if a mixture is lean or rich is the equivalence ratio (ϕ), defined as

$$\phi = \frac{(A/F)_{stoic}}{A/F}, \tag{2.5}$$

with A/F being the actual air-fuel ratio present in the mixture. It follows that for a lean mixture $\phi < 1$, and for a rich mixture $\phi > 1$.

In rich conditions you will always have incomplete combustion. Because there is an insufficient amount of oxidants present there will always be leftover fuel. As a result, the leftover fuel can react with other reaction products producing soot [27], or otherwise just diffuse away and be lost. As such, burning a rich mixture is generally fuel-inefficient.

In a lean mixture chances of complete combustion are higher, meaning the process is more fuel-efficient. However, it may lead to combustion instability [28, 29], and higher combustion ignition temperatures, due to the change in molecular compositions affecting the internal energy exchange. Higher ignition temperatures can result in more NO_x emissions [30], and combustion instability can result in ignition difficulties and flame extinction [31].

2.2.2 Thermodynamics

A central term in combustion thermodynamics is the adiabatic flame temperature. If the enthalpy of the reactants before combustion is equal to the enthalpy of the products after combustion, the mixture burns adiabatically. In other words: it is the maximum temperature that can be reached by the reaction products.

A temperature lower than the adiabatic flame temperature may be caused by incomplete combustion, dissociation, and heat transfer to the surroundings, amongst other things. As such one can use the actual flame temperature as a quantitative measure of how well a combustion process goes, by comparing it to the adiabatic flame temperature.

As mentioned, the adiabatic temperature is dependent on the enthalpy of the reactants. Therefore, this can be directly correlated with the equivalence ratio, seeing as this is an expression of the exact quantity of species present (Fig. 2.4).

Another important thermodynamic definition that can be linked to the equivalence ratio is the flammability limit. The flammability limit refers to the minimum and maximum equivalence ratio necessary for a combustion process to self-sustain after ignition. Aside from equivalence ratio it also depends on pressure and temperature [33].

2.2.3 Fluid Mechanics

The fluid mechanics of combustion is generally centered around flame and species propagation, which can behave quite turbulently between ignition and extinction. This can be expressed with the burning velocity (which is the velocity with which a flame propagates relative to the reactants), or the flame speed (which is the propagation velocity relative to a fixed point of reference). Once again this is not a stand-alone mechanic operating in isolation. For example, the flammability limit directly affects the flame stability and hence can lead to less efficient combustion. However, seeing

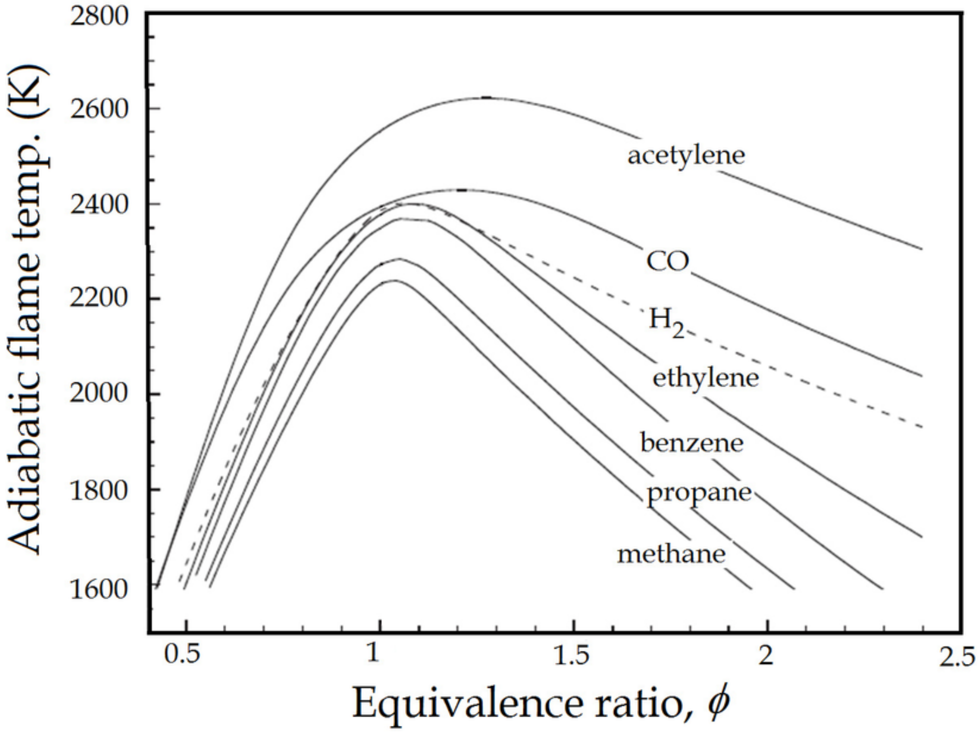

Figure 2.4. *A simulation of the adiabatic temperature for several gasses [32].*

as our current study is mostly interested in the thermodynamic aspects of ignition, most things regarding this topic will be left unspoken.

2.3 Plasma Assisted Combustion

One could say that plasma assisted combustion (PAC) was first observed in 1814, when Brande *et al* [34] researched the effects of an external electric field on fire. More concretely PAC entered the worldstage in 1860 with the invention of the sparkplug by Étienne Lenoir [35]. Indeed, this was in a time before plasma physics as its own discipline was even formally conceived by Irving Langmuir in the 1920s. However, with the knowledge of today this could be identified as humanity's preliminary attempt of combining combustion science with plasma physics in its quest to harness the flame.

In the past two decades research on PAC has increased due to its promising nature in making numerous aspects of combustion more efficient. In general these aspects can be categorised in the thermal enhancement pathway, the kinetic enhancement pathway, and the transport enhancement pathway. These pathways rarely operate on their own, and instead often reinforce each other. While this a great benefit to PAC, it also makes it more difficult to research. As such, it is all the more important to be at least partially aware of some of the different contributions [11, 36].

The thermal enhancement pathway refers to the mechanism where a plasma will produce additional heat, leading to an increased reaction rate according to the Arrhenius equation. A study by Elkholy *et al* (2018) [37] has shown that for their microreactor this was the leading enhancement pathway of their combustion process, contributing to about 90% of the enhancement of burning velocity. However it should be noted that the selectivity is poor, and this effect will accelerate the reaction rate of any reaction.

The kinetic enhancement pathway refers to chemical mechanisms made possible because of radicals and other reactive species in plasma. For example the added oxygen (O) and hydrogen (H) atomic radicals (and their excited states) will help the combustion process (as can be seen in Fig. 2.3). The production of ozone (O_3) in an air plasma can also be used to control combustion and ignition [38]. Having said that, introducing a plasma to an already intricate combustion process makes it a chemically complex melting pot. As such, this is one of the least understood enhancement pathways, both quantitatively and qualitatively. Improved species density measurements could prove fruitful in explaining this mechanism.

The transport enhancement pathway concerns the fluid mechanics of a plasma, and the effects thereof. An example is the production of ionic winds in a plasma, which can change the local flow velocity leading to increased mixing of reactants.

A combined effect of the thermal and kinetic enhancement pathway in the form of plasma assisted low temperature ignition has attracted more attention in recent years [39, 40]. Nanosecond pulsed dielectric barrier discharges have been found to decrease ignition delay. A decrease in ignition delay leads to higher thermal efficiency, while also leading to lower peak temperatures resulting in fewer NO_x emissions [41].

2.4 Spontaneous Raman Spectroscopy

Spontaneous Raman spectroscopy is a non-invasive laser diagnostics tool that can be used to determine the rovibrational energy state and species density of a molecule. This technique measures the frequency shift of inelastically scattered light on a molecule.

2.4.1 Molecular Energy Contributions

To better understand the process behind this scattering, and the physical interpretation of the observed frequency shift, we will first have a look

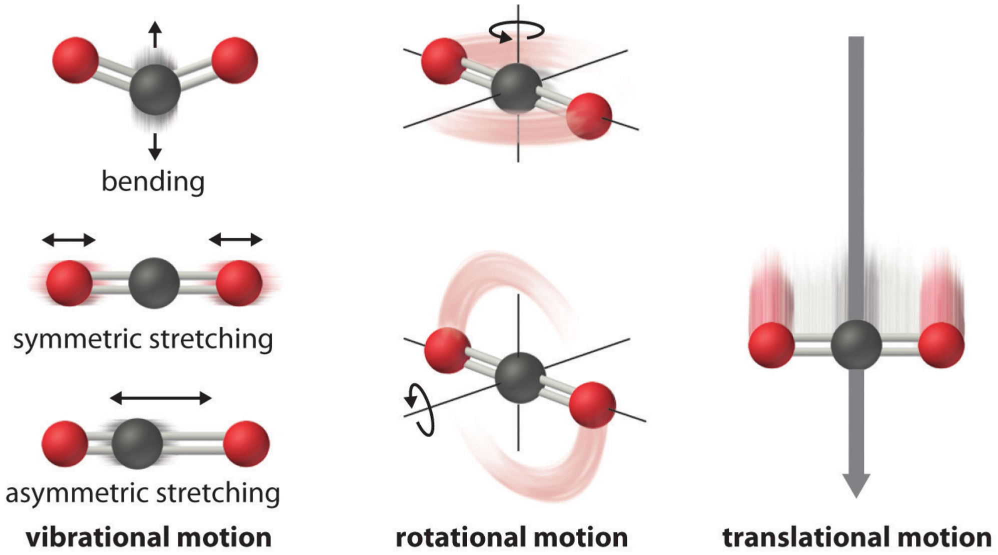

Figure 2.5. *Molecular motions of* CO_2 *[45].*

at the different internal energy contributions (degrees of freedom) of a molecule [42].

Firstly there is the translational energy which is used to express the energy due to motion of the molecule as a complete unit. This energy is a function of mass and velocity.

Secondly there are the inter-molecular energies. These become especially convoluted when considering a molecule that contains two or more atoms. This molecular energy ($E_{molecular}$) is often simplified by the Born-Oppenheimer approximation which separates the treatment of the motion of the nuclei and electrons within a molecule [43]. As a result the energy can also be treated to be a sum of terms that are assumed to be independent from one another:

$$E_{molecular} = E_{electronic} + E_{vib} + E_{rot} + E_{nuclearspin}, \tag{2.6}$$

with $E_{electronic}$ the electronic energy contributions due to electron-electron and electron-nucleus interactions, E_{vib} the vibrational energy due to bending and stretching of the bonds between nuclei of di- and poly-atomic molecules, E_{rot} the rotational energy due to rotation of an entire molecule, and $E_{nuclearspin}$ the angular momentum of individual particles [44]. A graphical representation of the physical meaning of vibrational, rotational and translational motions of CO_2 can be found in figure 2.5.

These different degrees of freedom of a molecule contribute significantly different magnitudes of energy, which can be categorised as $E_{electronic} > E_{vib} > E_{rot} > E_{nuclearspin}$. In fact $E_{nuclearspin}$ is so small it is often neglected altogether when trying to ascertain the energy of the molecule. All the other energy contributions are shown in figure 2.6.

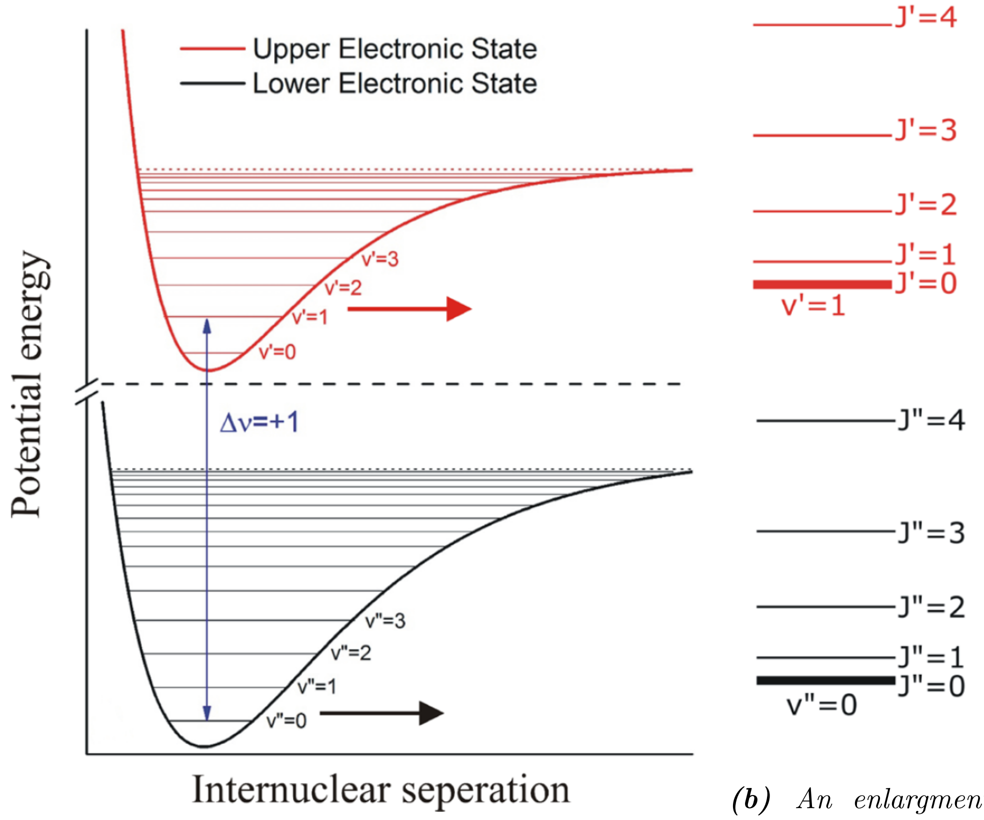

(a) *Some vibrational energy levels within an electronic state. The arrow signifies a transition between two electronic and vibrational states.*

(b) *An enlargment of the potential energy of rotational motion encaptured within a single vibrational state.*

Figure 2.6. *Energy diagram with some of the electronic, vibrational (v), and rotational (J) energy levels of a di-atomic molecule [46].*

Translational energy is not often the direct focus of spectroscopy [47]. Instead, it is sometimes assumed to be in equilibrium with the rotational temperature [48, 49, 50]. This assumption is based on the idea that rotational and translational energy exchange with their environment happens relatively fast, so they achieve thermal equilibrium at a faster rate than the vibrational energy. When considering Raman spectroscopy, one can additionally assume that the electronic energy levels are stable (because the diagnostics laser uses an off-resonant wavelength). This results in the conclusion that by merely measuring the subtle rovibrational temperatures one can get a surprisingly complete picture of a molecule's thermal state in a rather elegant way.

Additionally, in the case of a di-atomic molecule (such as N_2) the only vibrational motion that contributes to the vibrational energy is the stretching and compression of the one symmetrical internuclear bond. Referring to figure 2.5 one can imagine that for a di-atomic molecule there is no bending, and there is also no difference between symmetric and asymmetric stretching. As a result the vibrational motion can be approximated to behave as a simple harmonic oscillator, which greatly simplifies the analysis of the vibrational energy [51, 52]. As a result di-atomic molecules are often the focus of Raman spectroscopy.

2.4.2 Raman Scattering

As described in the previous sections, energy levels are quantized, meaning they differ in discrete steps from one another. However, photons with off-resonant energies can still interact with a molecule upon impact. The scattering process of an off-resonant photon with a molecule is often described as a two-photon process where the molecule instantaneously absorbs one photon and emits another, simultaneously. The absorbed photon elevates the molecule to an (infinitely temporary) virtual state, and the emitted photon allows the molecule to fall back to a discrete energy-state.

When the new energy-state is the same as the pre-collisional energy state we speak of Rayleigh scattering. In this case the photon's energy is conserved during scattering, which is what happens most of the time. However, sometimes the molecule falls back to a different energy-state which also results in the scattered photon possessing a different energy than the original impacting photon. When this happens we speak of Raman scattering. A graphical representation of this phenomenon can be seen in figure 2.7.

Upon realising that the energy of a photon is expressed as $E = \frac{hc}{\lambda}$, with h Planck's constant, c the speed of light, and λ the wavelength of the photon, the energy difference between the colliding (E_c) and the scattered photon (E_s) can be expressed as a function of their wavelengths as

$$E_c - E_s = \frac{1}{\lambda_c} - \frac{1}{\lambda_s}. \tag{2.7}$$

The energy difference of equation 2.7 is directly related to a specific (ro)vibrational transition. Seeing as the wavelength and frequency of a photon are intrinsically tied together by the speed of light, it should now slowly become clear how measuring the frequencyshift of the scattered light supplies valuable information about the energystate of the impacted molecule.

Rayleigh scattering is about 3 to 4 orders of magnitude more intense than Raman scattering [54]. Therefore, when trying to measure the Raman signal for spectroscopy purposes, the Rayleigh signal is usually filtered out.

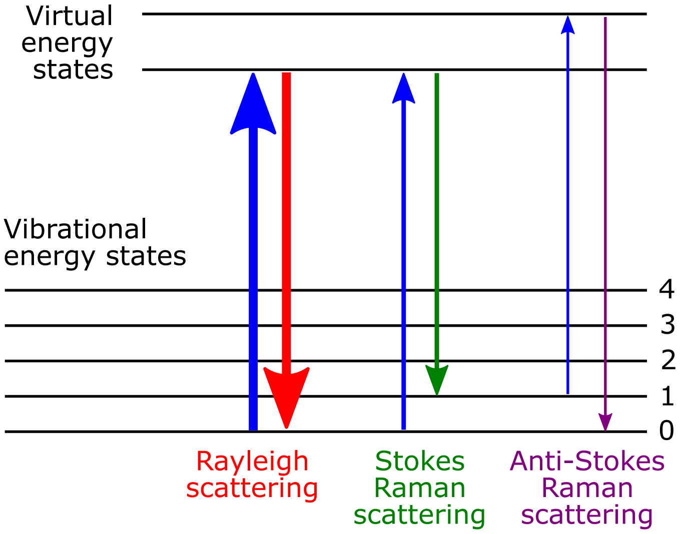

Figure 2.7. *Graphical representation of Rayleigh and Raman scattering [53]. Depending on the post-collisional state of a molecule we speak of Stokes Raman scattering when energy is absorbed by the molecule, and Anti-Stokes Raman scattering when energy is emitted.*

What you are left with are the inelastically scattered photons with either higher or lower energy than the incident photon, specifically called Anti-Stokes and Stokes Raman scattering, respectively.

Raman scattering occurs when an incoming electromagnetic field (such as light) is presented with a rotating or vibrating molecule. This then changes the molecule's polarizability with respect to the light, causing an induced dipole, causing a (ro)vibrational transition [55]. This polarisability is dependent on the ease of distortion of the electron cloud of a molecule, and as such is very molecule dependent. As a result this gives rise to the Raman selection rules, which states that only very specific (ro)vibrational transitions of a molecule are possible when presented with an external electromagnetic field. For example, for a diatomic molecule the Raman selection rules state that the vibrational energy can only change by $\Delta \mathrm{v} = \pm 1$, and the rotational energy state by $\Delta \mathrm{J} = 0, \pm 2$. This property is another one of the golden nuggets that helps in analysing a Raman spectrum.

This thesis will not delve too deeply into the details of how the aforementioned aspects of Raman spectroscopy are combined and molded into a way to (computationally) analyse a Raman spectrum. If one is interested in such practices I refer to predecessor graduation students Hessels [56] and Pelders [57] who have developed and enhanced such analysation tools for combustion purposes.

That being said, it might be interesting to have a quick look at the following Raman intensity fitting equation [58] that is often the basis of such data analysis:

$$I_{Ram}^{\beta} = \sum_{\alpha} \sum_{i,m,n} \frac{d\sigma_{imn}^{\alpha\beta}}{d\Omega}(v_{imn}, \theta) \times F_{imn}(v - v_{imn}) \times \frac{g_{im} \times \exp(-\frac{hcE_{im}}{kT})}{Z_i(T)} \times N_i \times I_0^{\alpha}, \tag{2.8}$$

with $\frac{d\sigma_{imn}^{\alpha\beta}}{d\Omega}(v_{imn}, \theta)$ the differential crosssection of a Raman transition between quantum states m and n of species i, $F_{imn}(v - v_{imn})$ a Raman line profile function, g_{im} and E_{im} the statistical weight and energy of quantum state m, $Z_i(T)$ a partition function, N_i species concentration, T temperature, k Boltzmann constant, θ the angle between direction of propagation of incident radiation and direction of observation, α and β refer to polarization orientation relative to the scatter plain, and I_0 the intensity of the light used to irradiate the probe volume.

As becomes apparent, the Raman intensity of equation 2.8 is mostly a function of a collection of known molecular parameters, leaving the temperature and species concentration as the to-be-determined variables. This is the core of how a Raman spectrum can lead to valuable information about a molecule, making it an excellent spectroscopy tool.

This page is intentionally left blank

CHAPTER 3

Laser Pulse Stretcher

Previous experiments done by Pelders [57] on the setup by Elkholy [13] showed that adding a plasma to the combustion process caused a significant uncertainty to the Raman measurements. To improve the signal-to-noise ratio (SNR) of the Raman signal it was decided to use a high-power 10 Hz Nd:YAG laser (Quanta Ray PRO-270-10 [59]). In our case this new laser had energy pulses of approximately 700 mJ in 9 ns, instead of 20 mJ in 170 ns by the previous 3 KHz laser (Photonics Industry DM20-527 Nd:YLF [60]).

A better SNR can also lead to faster measurements, with some labs even reporting on single-shot Raman spectroscopy [14, 15]. This potentially allows us to analyse fast processes during combustion (such as the ignition of a flame by plasma streamers) or do species density measurements to explore the kinetic enhancement pathway of PAC.

However, all these benefits come at a cost. Focusing an Nd:YAG laser with the properties as mentioned may result in an optically induced breakdown. Optical breakdown was first discovered in 1963 (hand in hand with the invention of the Q-switched laser), and it came as a complete surprise for physicists at the time [61]. This exciting new discovery attracted a colossal interest from researchers around the world. Sadly, our interest mostly lies in thwarting optical breakdown from occurring. The spectroscopic signal of such a volatile plasma, and its unpredictable interaction with a combustion process, would interfere greatly with our actual measurements. The steps taken to prevent it from happening (while still maintaining a proper laser power for an effective Raman signal), will be described in this chapter.

Before proceeding it should also be mentioned that it was found that the energy deposition in space of the laser beam was no longer the even distribution it used to be upon purchase (Fig. 3.1). The current state

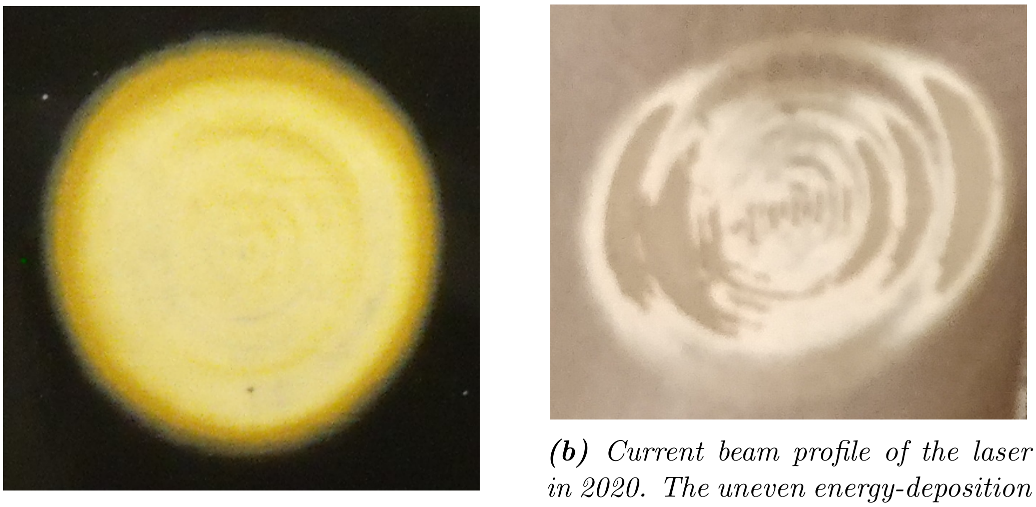

(a) *Beam profile of the laser upon purchase in 2012.*

(b) *Current beam profile of the laser in 2020. The uneven energy-deposition that is visible even damages high energy optics.*

Figure 3.1. *The beam profile of the Nd:YAG laser used for the experiments at two different points in its lifetime.*

of the laser caused damage to optical equipment (even the kind meant for high energies). As a result the laser beam was first directed into a lens-configuration consisting of a negative and a positive lens magnifying the beam diameter by a factor of 1.3 (to approximately 1.3 cm), which managed to prevent the aforementioned damage. Sadly, this also meant an increase in divergence of the laserbeam, which caused problems that will be addressed later on in this report.

3.1 Optical Breakdown Threshold

Optical breakdown at pressures greater than 10 Torr has been proposed to be caused by seed electrons gaining energy by inverse bremsstrahlung, resulting in an electron cascade process, eventually inducing a full breakdown [62]. The breakdown threshold depends on numerous factors such as the surrounding medium, ambient pressure, and optical power density.

To determine the breakdown threshold that was relevant to the setup, a quantitative analysis was performed. The laser was focused in a vacuum vessel cleaned from dust, and merely containing air at atmospheric pressure. This was done with a positive lens with focal length $f = 1\,\mathrm{m}$ (the same one that would eventually be used to focus the diagnostics laser in the probe volume). Seeing as the optical breakdown threshold has a negative dependence on pressure [63], measuring at 1 bar would give the outer limit for the purposes of this thesis.

From this experiment it was deduced that the optical breakdown threshold under the aforementioned conditions was $(1.5 \pm 0.1) \times 10^2$ mJ, or a pulse power of $P_{pulse,breakdown} = (1.7 \pm 0.1) \times 10^7$ W. With the knowledge that the full laser pulse power sits at $P_{pulse,full} = 7.8 \times 10^7$ W, this lead to the conclusion that the peak power of the laser needed to be reduced by a factor of 5.

For the purposes of this thesis the breakdown threshold in pure air was the only relevant consideration. However, if one wants to do Raman measurements on an active combustion process in the future, it is worth noting that the breakdown threshold in pure methane is about 75% to 85% [62] of that in air (depending on pressure). Of course, future experiments will rarely be in pure methane, instead it will always consist of quite a significant amount of air (especially in lean conditions). Still, one should take this into account when trying to determine an appropriate power density.

3.2 Pulse Stretcher Considerations

As a means to decrease the peak power of the laser (while maintaining as much of the total pulse energy as possible), a pulse stretching setup was build. Such a setup uses optical cavities (Fig. 3.2) to stretch out a single laser pulse over a longer time domain (Fig. 3.3). This way the full energy of the pulse (the full integral of the power versus time) is theoretically unaffected, while the peak power is significantly reduced. Such pulse stretchers have been applied to combustion experiments in the past [15, 64, 65].

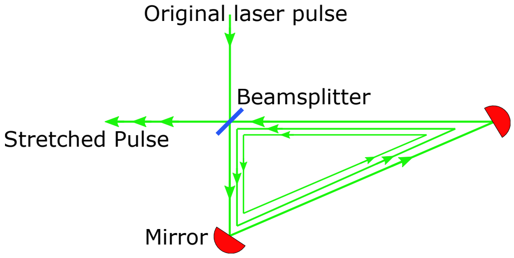

Figure 3.2. *An optical cavity meant to break the temporal power profile of a laser pulse into smaller, increasingly delayed, pieces. The cumulative output profile is directly affected by the beamsplitter reflectance, and the cavity path length.*

An optical cavity like this consists of a beamsplitter that will reflect one part of the laserpulse, and will transmit the other. The reflected part will be directed towards the probe volume, whereas the transmitted part will enter a system of mirrors before eventually ending up at the beamsplitter again. Here it will once again be split in two, however this time the transmitted part joins the initially reflected part (yet now slightly shifted in time), and the reflected part will be redirected into the system of mirrors once again, theoretically repeating the process *ad infinitum.* The time shift of the part of the laser pulse that gets bounced around inside the optical cavity is a product of the path length within this cavity and the speed of light. The final result will be a laserpulse where the original energy will be deposited over a longer period of time, hence decreasing the average power. This can be done with one such cavity, or one could build a system consisting of a multitude of these optical cavities for increased stretching.

According to a quantitative analysis on pulse stretchers by Kojima *et al.* (2002) [63] the effective reduction of the peak power depends on the amount of cavities placed after one another, the reflectance of the beamsplitters, the length of the cavities, and the length ratio of consecutive cavities. They found that the most efficient ratio of cavity lengths of consecutive optical cavities should be 2:1, with every added cavity doubling in length. The optimal beamsplitter reflectance is $R_{BS} = 40\%$, and the shortest cavity should have a path length of $L = cd_t$ (with c the speed of light, and d_t the original laser pulse width).

Assuming that the power-time profile of a laser pulse ($P(t)$) behaves approximately like a Gaussian, this profile can be expressed as a function of its full width at half maximum (FWHM) as

$$P(t) = \exp^{-4\ln(2)t^2/d_t^2}, \tag{3.1}$$

with t the time, and d_t the FWHM of the laser pulse (that is: the pulse width). From this it can be deducted that the effect of, for example, two optical cavities on the power-time profile can be expressed as a summation of increasingly time-shifted exponential functions as

$$\begin{aligned} P_{stretched}(t) = & R_{bs}^2 \exp^{-4\ln(2)t^2/d_t^2} + \\ & (1-R_{bs})^2 (\sum_{i=1}^{n} R_{bs}^i \exp^{-4\ln(2)(t-i\frac{L_1}{c})^2/d_t^2} + \\ & \sum_{j=1}^{m} R_{bs}^j \exp^{-4\ln(2)(t-j\frac{L_2}{c})^2/d_t^2}) + \\ & (1-R_{bs})^4 \sum_{i=1}^{n} \sum_{j=1}^{m} R_{bs}^{i+j-2} \exp^{-4\ln(2)(t-i\frac{L_1}{c}-j\frac{L_2}{c})^2/d_t^2}, \end{aligned} \tag{3.2}$$

with n and m the amount of iterations through the first and second cavity respectively (must be greater than or equal to 1), L_1 and L_2 the path lengths of the first and second cavity respectively, and c the speed of light. If either m or n is 0, then the last term with the double summation has to be removed, and the summation dependent on the iteration that is 0 has to be removed.

Similar expressions for the stretched power-time profile such as in equation 3.2 have been made for a system with one and three cavities. These have subsequently been plotted (Fig. 3.3) for $R_{bs} = 0.4$, 50 iterations within

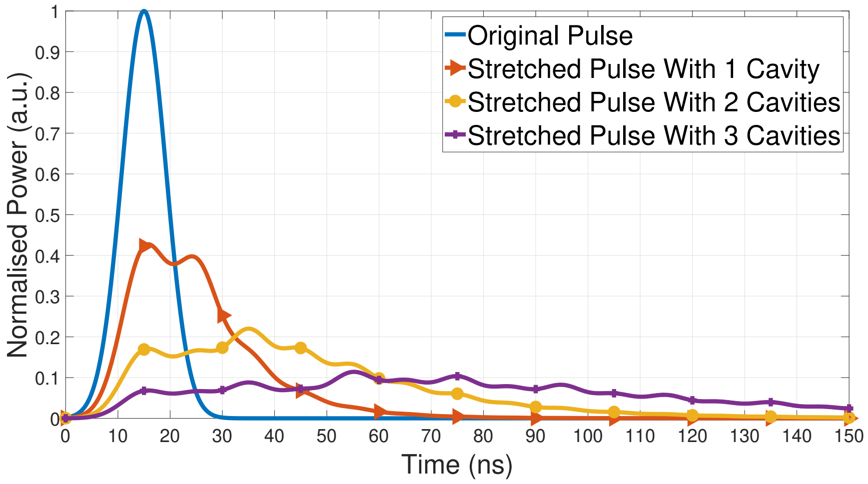

Figure 3.3. *The calculated power-time profile under the influence of zero, one, two, and three optical cavities as in Fig. 3.2. The area under each curve (that is: the energy) is the same for all.* $R_{bs} = 40\%$*, the shortest cavity length is* $3\,\mathrm{m}$ *(based on a pulse width of* $10\,\mathrm{ns}$ *of the original pulse), and every added cavity increases in length by a factor 2.*

each cavity, $d_t = 10\,\mathrm{ns}$, path length $L_1 = 3\,\mathrm{m}$, and every potential added cavity increasing in path length by a factor of 2.

From this calculation it was found that to achieve the desired 5 times reduction in peak power, a pulse stretcher consisting of two optical cavities was required. Specifically a two cavity system would lead to 22.4% peak power compared to the original pulse.

To finalise the decision on the exact design of a pulse stretcher suitable for this study, the different tuneable parameters of equation 3.2 were further explored. This eventually led to the design showcased in Fig. 3.4, with 2 inch beamsplitters ($R_{BS} = 40\%$), $L_1 = 5.05\,\mathrm{m}$, and $L_2 = 3.15\,\mathrm{m}$. As mentioned at the start of the chapter a 'telescope' consisting of a negative ($f = -75\,\mathrm{mm}$) and a positive ($f = 100\,\mathrm{mm}$) lens in an afocal configuration was used. This resulted in a 1.3 times magnification to prevent damaging equipment. Lastly, a half waveplate (HWP) was implemented to adjust the laser polarisation before going into the setup.

The theoretical maximum energy transmission of this system can be calculated by considering the reflection efficiency of each mirror. When m

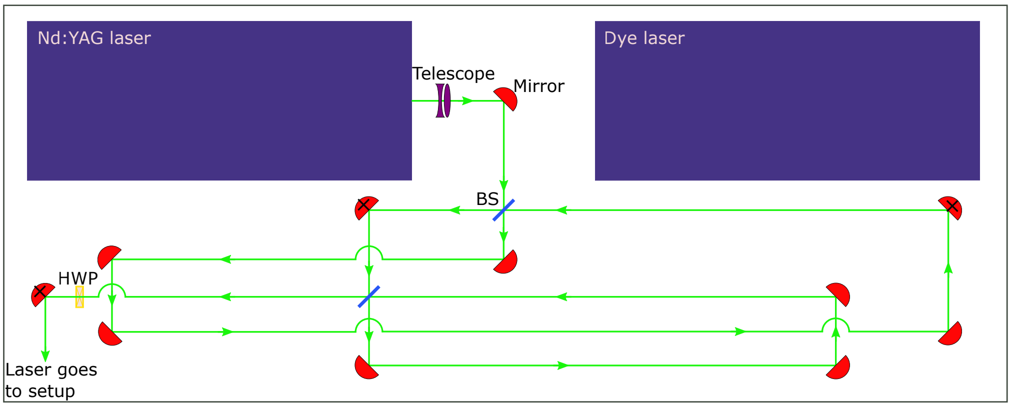

(a) *A sketch of the pulse stretcher build for the diagnostics laser. Components are a lens configuration to enhance the beam diameter (Telescope), two 2 inch beamsplitters (BS), mirrors, and a half waveplate (HWP). The mirrors with a cross are 2 inch in diameter, the others 1 inch.*

(b) *The pulse stretcher in action.*

Figure 3.4. *The final pulse stretcher design. The dye laser can be used in combination with the Nd:YAG laser to perform planar laser-induced fluorescence (PLIF) measurements, but that was not attempted during this study.*

and n are greater than or equal to 1 this can be expressed as

$$\begin{aligned}E_{trans} =& T_{tel} R_{m,2} T_{HWP} R_{bs}^2 + \\ & (1-R_{bs})^2 \left(\sum_{i=1}^{n} (R_{m,1}^3 R_{m,2}^2 R_{bs})^i + \sum_{j=1}^{m} (R_{m,1}^3 R_{bs})^j\right) + \\ & (1-R_{bs})^4 \sum_{i=1}^{n} \sum_{j=1}^{m} R_{bs}^{i+j-2} (R_{m,1}^3 R_{m,2}^2)^i (R_{m,1}^3)^j,\end{aligned} \tag{3.3}$$

with $T_{tel} = 0.995$ the transmission of the telescope, $T_{HWP} = 0.9975$ the transmission of the HWP, and $R_{m,1}$ and $R_{m,2}$ the reflection of the two types of mirrors used. One type of mirrors was purchased for this setup and posses a known reflection of $R_{m,2} = 0.99$. However, the other mirrors that are used are from unknown origins, and as such the mirrors with the worst reflections from the Thorlabs website are assumed, resulting in $R_{m,1} = 0.98$. If either m or n is 0, then the last term with the double summation has to be removed, and the summation dependent on the iteration that is 0 has to be removed.

If we assume perfect alignment resulting in $n = m = \infty$, the maximum energy transmission achieveable is $E_{trans} = 87.0\%$. In reality, however, slight misalignments and beam divergence leading to bigger beam diameters than mirror diameters will result in additional energy loss. This will be explored more thoroughly in section 3.3.

In case the reader is interested in a practical 'how-to' guide on building (or maintaining) a pulse stretcher like this: appendix A has been written for this purpose.

3.3 Pulse Stretcher Analysis

Focusing the laser with a $f = 1\,\mathrm{m}$ lens, after stretching it with the pulse stretcher in Fig. 3.4, had a clear effect on the optical breakdown frequency. At pressures below 1 bar it was reduced to frequencies less than once per minute. Additionally it was clearly seen that nearing 500 mbar (and lower) the optical breakdown frequency neared 0. This was the main purpose of the pulse stretcher, and as such could be seen as a success.

However, evaluating Fig. 3.4 one can imagine that physically building a setup like that (with two infinitely iterative mirror systems) is hardly trivial. As such, it was deemed necessary to more concretely analyse the effect of the pulse stretcher before proceeding to do Raman measurements. Firstly, the relative energy transmission was investigated. Secondly, the effect on the time domain was explored.

3.3.1 Energy Transmission

To research the relative energy transmission, a power meter was placed at the location of the HWP in Fig. 3.4. The energy was measured for both cavities closed, for each cavity individually, and for both cavities open. Additionally the transmitted energy as a percentage of the full laser energy (700 mJ), and the theoretical maximum under the same conditions from equation 3.3 were calculated (table 3.1).

With both cavities opened it was noted that of the original $7 \times 10^2\,\mathrm{mJ}$ approximately $(54 \pm 1)\,\%$ ($(3.80 \pm 0.05) \times 10^2\,\mathrm{mJ}$) reached the end. This is about 33 percent points lower than the calculated $E_{trans} = 87.1\%$ in

Table 3.1: Cavity energy transmission of the pulse stretcher of Fig. 3.4.

Opened cavity	Measured pulse energy (mJ)	Percentage of total energy (%)	Expected percentage with perfect alignment (%)
Closed cavities	105 ± 5	15	15.6
First cavity	205 ± 5	29	37.3
Second cavity	202 ± 5	29	35.8
Both cavities	380 ± 5	54	87.0

section 3.2. This discrepancy is firstly attributed to imperfect alignment of the optical cavities, leading to a part of the laserlight getting irrevocably lost after a certain amount of iterations. A second cause is the laserbeam becoming too big in diameter due to its divergence (enhanced even further by the telescope) and subsequently reflecting off 1 inch mirrors at a 45°angle (leading to an effective reflective surface of only $\frac{1}{\sqrt{2}}$ inch). All the 2 inch mirrors that were found in the lab have been used, but sadly there weren't enough and a lot of energy was still lost.

Additionally it was seen that the first and second cavity had a very similar transmission efficiency. Theoretically the second cavity should be slightly better because of the fewer mirrors and the shorter path length. However, the near unnoticeable difference could imply that the first cavity is simply slightly better aligned.

Comparing this to literature, other labs have managed to achieve higher transmissions. For example Fuest (2011) [15] has reported on a 75% energy transmission for a three-cavity system by using 2 inch mirrors in motor-driven mirror mounts guided by CCD cameras to actively govern cavity alignment. Hoffmeister (2015) [65] similarly has a 75% transmission for a three-cavity system, however the exact circumstances of their setup are unknown. Geyer (2004) [64] reports on a 80% transmission for a two-cavity system similar to ours. The difference between his setup and ours lies in his use of 2 inch mirrors, and CCD cameras to monitor alignment. Last but not least, none of them suffer from quite the same beam diameter and divergence as us, seeing as they have no need for a telescope.

To conclude, future recommendations to improve the energy transmission would be to fix the beam profile of Fig. 3.1b, so that the telescope can be eliminated from the setup. This would result in a smaller beam diameter and a smaller divergence of the laser throughout the entire setup. Additionally upgrading to bigger mirrors would be beneficial for capturing more of the laser beam within the system. Lastly one could improve the alignment of the cavities by applying a steadier hand to the setup, or perhaps even by upgrading to computer-guided mirror mounts.

3.3.2 Time Stretching

To investigate the effect of the pulse stretcher on the time domain of a laser pulse, the expected effect was first calculated by using equation 3.2. Applying $R_{BS} = 40\%$, $d_t = 9\,\text{ns}$, $L_1 = 5.05\,\text{m}$, and $L_2 = 3.15\,\text{m}$ Fig. 3.5a was produced. This figure shows the expected power-time profile at the location of the HWP when both cavities are closed, when only the first cavity is opened, and when both cavities are opened. Afterwards, the actual power-time profile was measured at this point under these conditions with a 2 GHz photodiode [66] and a 400 MHz oscilloscope [67], averaging over 50 sweeps (Fig. 3.5b).

Comparing both images in Fig. 3.5 it can be seen that with every iteration within a cavity the measured power becomes lower than what the relative power would be in case all the energy was preserved (as per the calculated curves). This is essentially due to the same reasons that the measured E_{trans} in the previous section is not 100%: imperfect reflections/-transmissions, imperfect alignment, big beam divergence, and small mirror diameters.

Comparing the images qualitatively it can be seen that the first cavity is aligned up to at least 3 iterations within itself, however the third peak (and most likely any peak after this) has so little of the energy conserved that it can be rendered useless for Raman spectroscopy purposes. The alignment of the second cavity can be gathered by counting the peaks that the "Pulse With Both Cavities" has on top of the "Pulse With One Cavity" curve. This leads to the conclusion that the second cavity has up to 4 iterations aligned, although the energy in the last two iterations is so small it can be neglected for any use in Raman Spectroscopy.

Interestingly: using equation 3.3 to calculate the theoretical maximum energy transmission of only 3 aligned iterations per cavity, this percentage comes to 81.8%. This is very close to the 87.0% of perfect alignment, which can be visually interpreted by the small areas of the peaks belonging to iterations above 3 in the calculated curve of Fig. 3.5a. This leads to the conclusion that the energyloss detected in the system presented here can be more so attributed to equipment and beamprofile, rather than alignment.

Furthermore it can be calculated from the measured profile that 92% of its total pulse energy is contained within the 40 ns domain ranging from 5 ns to 45 ns in Fig. 3.5b. This is done by comparing the area of this domain with the total area of this curve. Going forward this value is now assumed to be the new pulse width of the stretched pulse.

From section 3.3.1 it is known that $E_{trans} = (54 \pm 1)\,\%$ $((380 \pm 5) \times 10^2\,\text{mJ})$, which would imply that the full integral of the "Pulse With Both Cavities"-line in Fig. 3.5b should also be in the order of $(54 \pm 1)\,\%$ of the full integral of the same line in Fig. 3.5a. However, an exact quantitative comparison

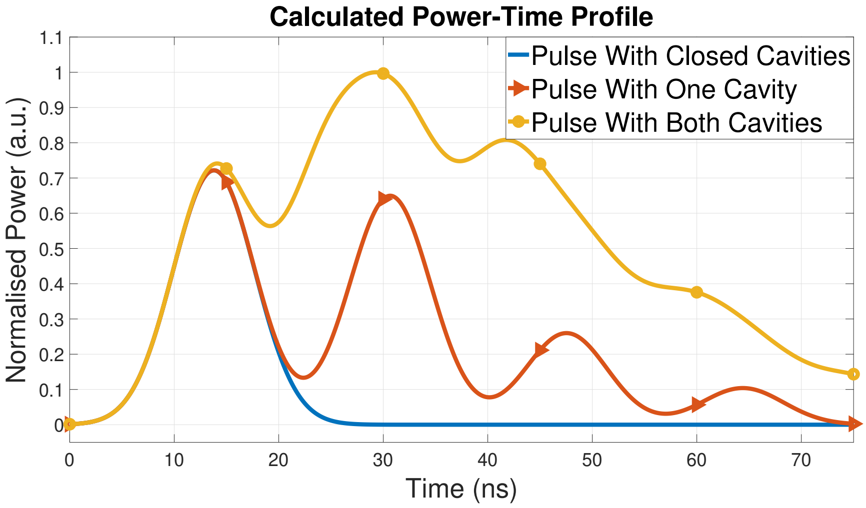

(a)

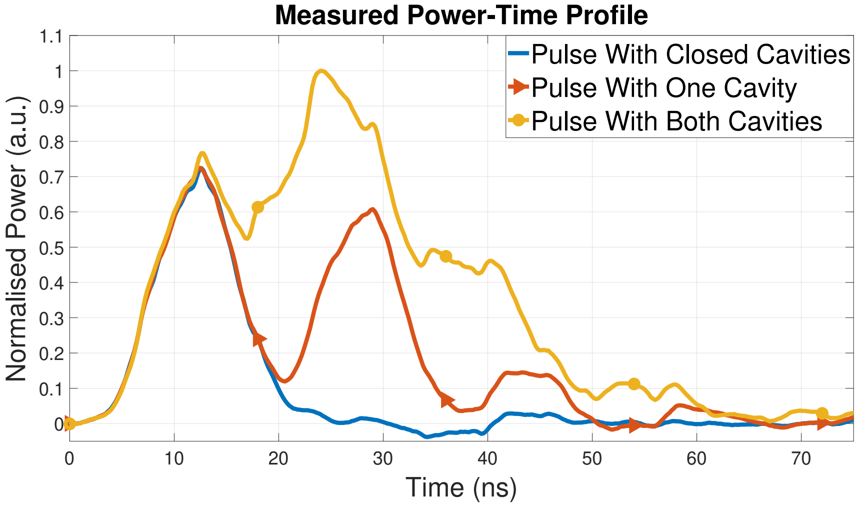

(b)

Figure 3.5. *The calculated (a) and measured (b) effect of the two cavity pulse stretcher on a laser pulse at the position of the half waveplate in Fig. 3.4. In both cases* $R_{BS} = 40\%$*,* $L_1 = 5.05\,\mathrm{m}$*, and* $L_2 = 3.15\,\mathrm{m}$*.*

between the areas underneath these profiles (meaning: the energy) was not attempted. The discrepancy between the shape of the calculated pulse, assumed Gaussian, and the actual pulse shape was deemed too big to allow for any sensible calculation in this regard.

All in all it can be concluded that the presented combination of Nd:YAG laser and pulse stretcher results in a $(3.80 \pm 0.05) \times 10^2$ mJ 40 ns laser pulse with an average power of approximately $P_{pulse,new} = (9.5 \pm 0.1)$ MW. Comparing this with the previously used Nd:YLF laser's power ($P_{pulse,old} = 0.12$ MW) it can be concluded that the pulse power has increased by about 80 times. That being said, it should be noted that because of the difference in pulse frequency (10 Hz versus 3 KHz), the average power of the previous laser is still about 3 times higher. This leads to the conclusion that while this new setup should lead to a better SNR, it will not necessarily lead to faster measurements.

3.4 Abandoned Designs

The story so far may imply that what has been presented was the destination envisioned at the start, and that the process leading up to it was all smooth sailing. While it's true that the general idea and application of the pulse stretcher has remained largely unchanged from beginning to end, the exact design and implementation has been reshaped continuously throughout the entire project. Some of the earlier designs (and why they were abandoned) are summarised in appendix B. If the reader is only interested in success stories, this appendix can be skipped. However, if one has any intention of recreating a similar setup, reading about the faults presented in this appendix may proof useful.

This page is intentionally left blank

CHAPTER 4

Experimental Setup

After the diagnostics laser passes through the pulse stretcher described in chapter 3, it will be directed into the actual experimental setup with a lens with focal length $f = 1\,\mathrm{m}$. The additional components of the experimental setup and the data analysis tools will be described in this chapter.

4.1 Vacuum Chamber

The main part of the action takes place inside a vacuum chamber designed by Ravi Patel (Fig. 4.1). It has a brewster window where the diagnostics laser can enter the vessel (A) and another brewster window with beam-dump where it can exit (B). Additionally it has an electrode connected to a high voltage generator coming in from the top (C), and a ground electrode connected to the bottom (D) (section 4.2). There is a window on the front side for the experimentalist to look inside during measurements (E), and a window on the far side through which the Raman signal is collected by a spectrograph (section 4.3).

There is also a flowtube connected to the left side of the vacuum vessel (F). This flowtube is connected to a compressed air reservoir, and the exact flowrate can be adjusted to values up to 5 standard litre per minute (SLPM). For combustion experiments (which are not attempted in this thesis), there is also a methane reservoir that can be used to create a premixed flame with any desired equivalence ratio. The only way for any species to leave the closed vacuum vessel is by being pumped out on the top right side (G) by a Kashiyama NeoDry15E vacuum pump [68]. This pump is used together with a Pfeiffer RVC300 Vacuum Control unit [69] to regulate the pressure.

The advantage of this setup is that the plasma and flame can be mixed

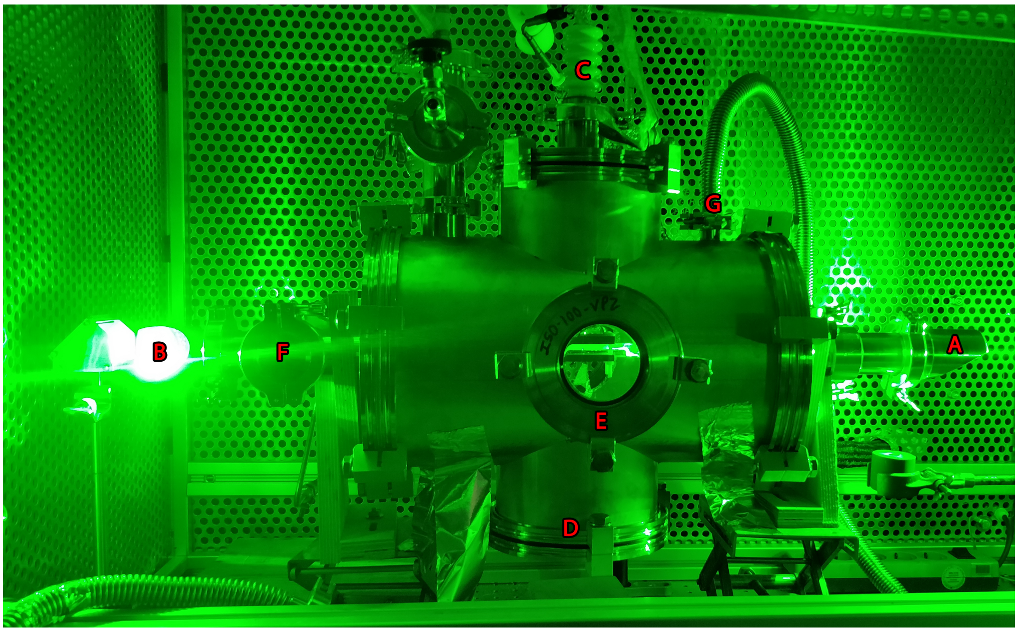

Figure 4.1. *The vacuum vessel in which the experiments take place (diameter 25 cm). The main components are (A) entrance of laser, (B) beam-dump, (C) high voltage supply, (D) ground electrode connection, (E) observers window, (F) flow input, and (G) flow output by pump.*

together, which was not possible with an earlier microreactor made by Elkholy [13]. This allows for plasma assisted combustion ignition, and also direct (Raman) measurements of the plasma and its effect on the surrounding molecules.

4.2 Dielectric-Barrier Discharge

The dielectric-barrier discharge configuration consists of a stainless steel high voltage (HV) top electrode touching a quartz plate (held together with epoxy resin), followed by an open air gap of 8 mm, and finally a tungsten ground electrode on the bottom (Fig. 4.2). This configuration is placed exactly in the middle of the vacuum vessel of Fig. 4.1.

The Megaimpulse NPG-18/3500 high voltage supply [70] that is used can produce up to 40 kV, with 30 mJ pulse energies. However, at the moment the exact voltage that eventually reaches the electrode (and as such the precise plasma characteristics) are unknown. As of writing there is a student working on figuring this out (Rick Peelen), which is not a trivial task due to energy losses outside of the vacuum vessel. These losses are caused by unwanted discharges outside of the vessel, and also by the voltage probe draining some energy. Additionally some energy is simply dissipated

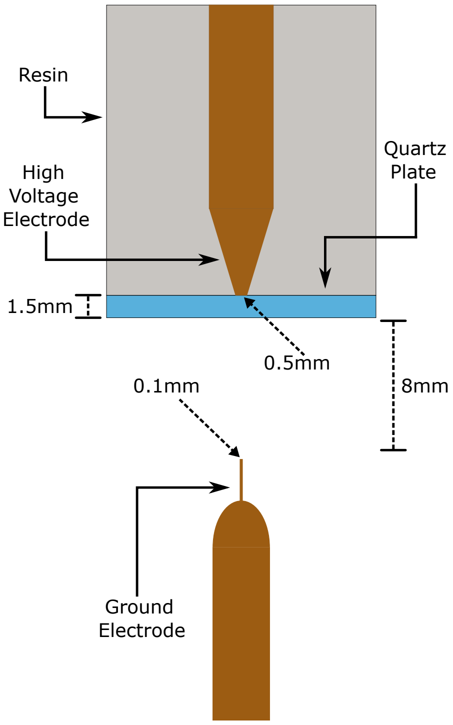

Figure 4.2. *The dielectric-barrier discharge configuration.*

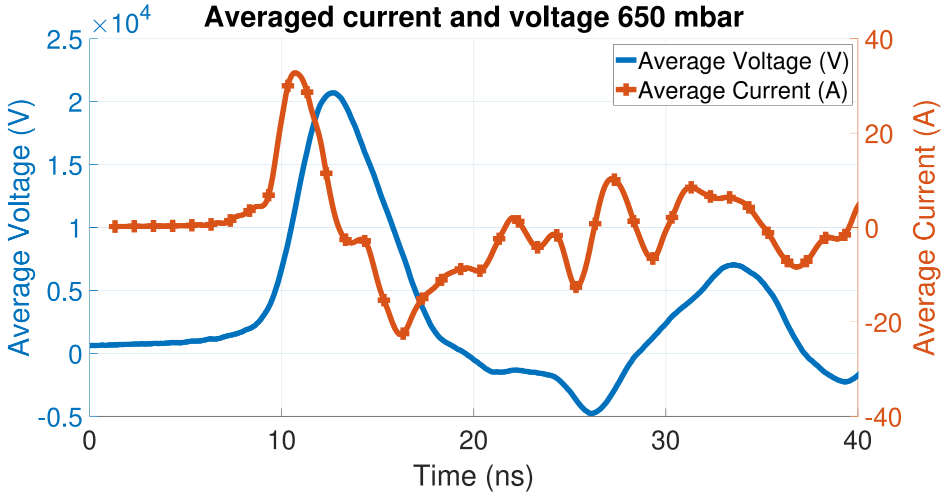

Figure 4.3. *Voltage-current measurement of the high voltage electrode in Fig. 4.2 by Rick Peelen. Averaged over 354 single measurements.*

through the cable that transports the pulse from generator to electrode.

That being said, some preliminary measurements (at 650 mbar) have come in and can be found in Fig. 4.3. It can be seen that the pulse voltage is in the order of 20 kV, rise time 4 ns, and a duration of 5 ns FWHM. From this the pulse energy E_{pulse} can be calculated by integrating over

$$E_{pulse} = \int_{t1}^{t2} P(t)dt = \int_{t1}^{t2} I(t) \cdot V(t)dt, \tag{4.1}$$

with $P(t)$ the power from time t_1 to t_2, which depends on the current $I(t)$, and voltage $V(t)$. From this computation it follows that $E_{pulse} = 4\,\mathrm{mJ}$.

Last but not least the pulse repetition rate is fixed at 3 kHz. Combined with the high voltage this leads to significant electromagnetic interference throughout the lab. To prevent this from happening the HV supply and the cable leading towards the electrode have been fully shielded.

4.3 Data Acquisition

Once the diagnostics laser strikes the probe volume, the scattered light will first go through an Edmund Optics OD4 532 nm notch filter [71] (to filter out Rayleigh scattering). Then it will pass through a 105 mm lens (focused on the plasma) mounted with a 10 mm extension ring on a (reflection grating) Princeton Instruments Acton SP-500i 0.5 m spectrograph [72]. It will enter this spectrograph through a slit parallel with the laser. This spectrograph has three available gratings: 300, 1200, and 2400 grooves/mm. Unless stated otherwise the 2400 grooves/mm is used for all experiments to maximize spectral resolution. After the spectrograph disperses the light, it is directed into an ICCD camera (Princeton Instruments PI-MAX 3, Filmless UniGen II intensifier) [73], from which the data can be read with Princeton Instruments WinSpec32 software [74].

All of these tools are synchronised with the help of two Rigol DG1032Z [75] pulse generators in order to maximise SNR. The first pulse generator triggers 2 things: the camera and the second pulse generator. The second pulse generator then goes on to trigger the diagnostics laser and the plasma pulse. Lastly, all the output triggers of every device were actively monitored with a LeCroy WaveRunner 44MXi-A oscilloscope [67]. Any synchronisation errors caused by signal travel time through cables and equipment-specific peculiarities, were ironed out by applying individual trigger delays.

For Raman measurements the gate width of the camera was set at 125 ns. To reduce noise capture, a value close to the 40 ns of the laser is preferred. However, the laser did not have a stable starting point. It was possible to synchronise the camera and laser to some extent, but even when triggered from the same signal the laser possessed some inherent jittering in between pulses leading to the laser pulse jumping around in time by about ±40 ns.

It was also possible to operate the camera with just the imaging mode turned on (that is, without the spectrograph's interference of the gathered signal). With that setting the vertical direction is expressed in pixels, which was used to determine the total slit length before experiments. This was done by placing an image with known dimensions at the focus point of the camera lens (Fig. 4.4). The horizontal axis usually denotes the wavelength when gathering data, but when the imaging mode is turned on it simply says that its centered around 0 nm. In reality the horizontal axis dimensions turn to pixels in imaging mode. The dots in Fig. 4.4 are (0.95 ± 0.05) cm apart from the top of one dot to the bottom of the other. It follows that the slit length (the red area in Fig. 4.4) is in the order of (1.6 ± 0.1) cm. Future images made with the imaging mode will have axes adjusted to this value.

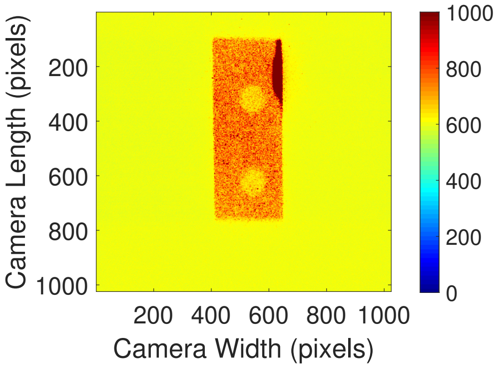

Figure 4.4. *An image placed in front of the camera to determine the slit length. The colour scale is based on signal intensity.*

4.4 Data Analysis

After the Raman signal is gathered it will look as in Fig. 4.5a. This figure shows the wavelength data on the horizontal axis, and also the vertical strips which are the pixels of the camera. Because of the orientation of the camera and the spectrograph, the vertical direction in Fig. 4.5a is in reality the horizontal direction in parallel with the laser.

Before this can be properly analysed, noise will have to be reduced by also performing a background measurement with the laser turned off (Fig. 4.5b), to subtract from the raw data. This way only the Raman signal should be left. Additionally a Hampel filter will be applied. A Hampel filter is similar to a median filter, except it has an added parameter with which the aggressiveness of the filter can be tuned. This tuning takes place on a spectrum with one end being the same as a median filter, and the other end meaning no filtering takes place [76].

After this has been done the data will be binned in the vertical direction

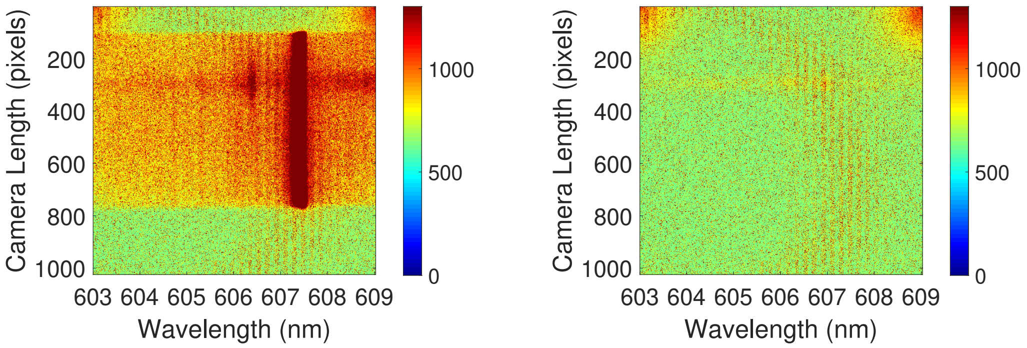

(a) *Raw measurement data.* ***(b)*** *Background data.*

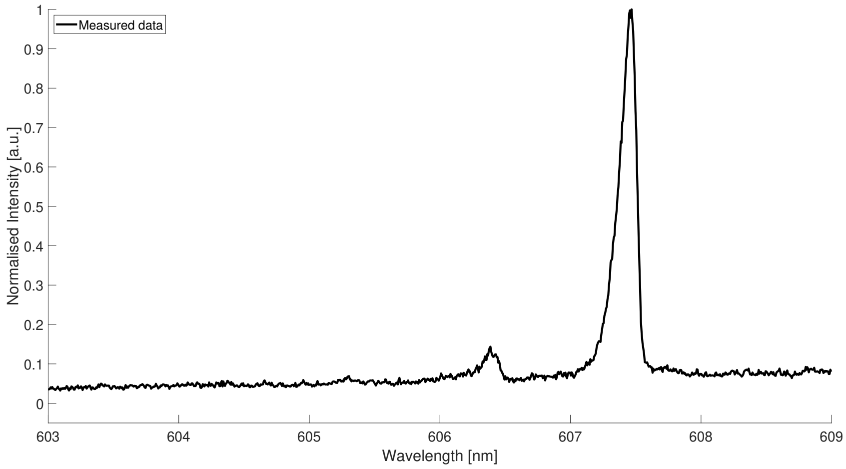

(c) *The Raman spectrum binned over vertical pixel 250 to 350 in Fig. 4.5a, after application of a Hampel filter and subtraction of the background data.*

Figure 4.5. *Data for a measurement* 200 ns *after a plasma discharge at 100 mbar.*

over 100 pixels. Figure 4.5c shows an example of the created spectrum, when it is binned from pixel 250 to 350 (the location of the plasma).

Theoretically one would expect to see an exact straight spectral line at the location of the Raman wavelength. Instead a curve is presented. The reason for this curve is line broadening, caused by uncertainty in the exact photon energy (due to Heisenberg's Uncertainty principle), the Doppler effect caused by the light source's relative velocity compared to the observer, and pressure (collisional) broadening caused by colliding molecules causing unpredicted energy exchanges. Additionally there are mechanical errors in the optical alignment both inside and outside of the spectrograph leading to a misinterpreted wavelength.

To properly process the line broadened data an instrumental function was used. This is a function (chosen by the experimentalist) meant to represent all the effects described in the previous paragraph. For the analysis done in this thesis a Gaussian function was chosen, with a FWHM of 0.11 nm, based on the Rayleigh image.

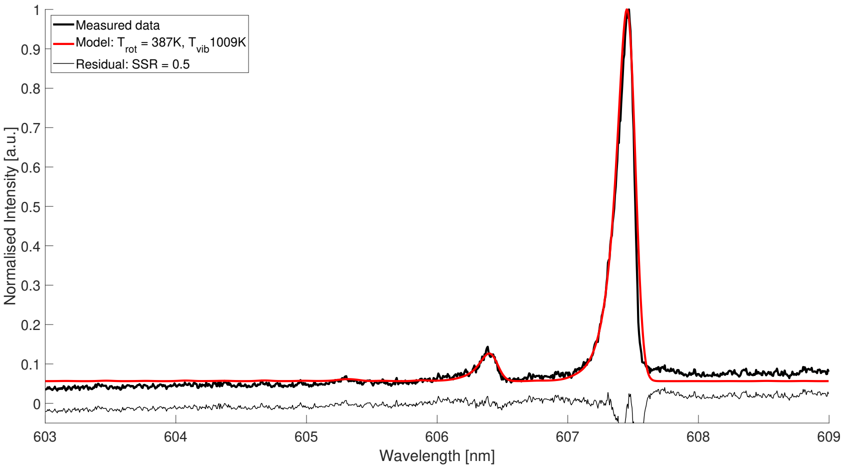

(a) *Two-temperature Boltzmann fit of the measurement data, and the (sum of squared) residuals.*

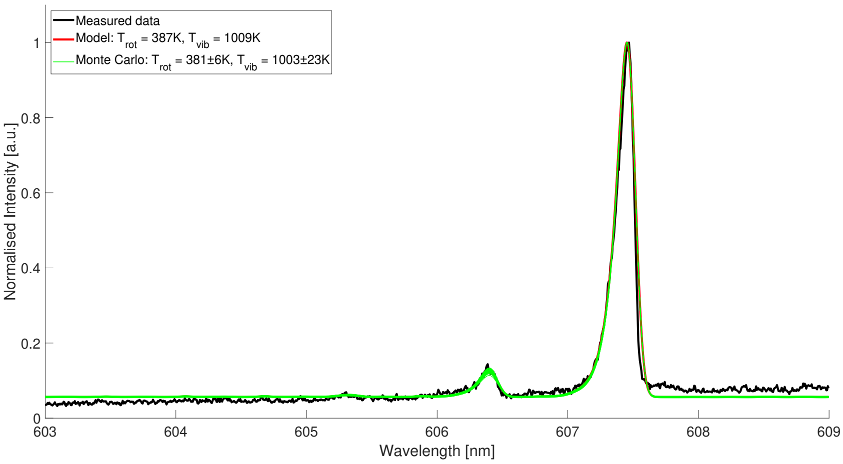

(b) *Uncertainty determination with the help of 20 Monte Carlo simulated experiments.*

Figure 4.6. *Data analysis for a measurement* 1 µs *after a plasma discharge at 100* mbar.

This measurement data was then be fitted with a two-temperature Boltzmann least squares fitting model developed by Hessels [56] and Pelders [57]. In summary this model applies separate partition functions for the rotational and vibrational population distribution, leading to a separation of rotational and vibrational temperature contributions (Fig. 4.6a). This is based on the idea that rotational relaxation happens faster than vibrational relaxation.

Uncertainties were determined with a Monte Carlo method, based on the residue between measured data and fitted model (Fig. 4.6b). From this residue a probability function is obtained, which is then used to generate a simulated experimental measurement. This simulated measurement is subsequently also fitted with the model, obtaining a new temperature. This can be repeated any number of times, after which an uncertainty is determined based on the different (simulated) temperatures. 20 of such Monte Carlo simulations per measurements were used for the measurements presented in this thesis.

Any SNR values presented in the experimental results were produced with the snr() function of MATLAB, which computes the ratio of the summed squared magnitude of the signal versus the noise. This ratio has decibel as unit.

This page is intentionally left blank

CHAPTER 5

Experimental Results

The Raman measurements performed with the pulse stretched laser will be presented in this chapter. For all measurements nitrogen (N_2) was chosen as the subject molecule. The reason for this is the prevalence of nitrogen in air, meaning it is a good molecule to represent the gas temperature. The relatively high species density also leads to a relatively strong Raman signal. Additionally, as mentioned in section 2.4, a diatomic molecule allows for easier temperature modelling.

5.1 Exploration of Rovibrational Temperature Measurements

5.1.1 Experiment Description

Some preliminary experiments have been performed to try out the use of the new laser in combination with the pulse stretcher. A single laser shot, a 10 shots, and a 1000 shots measurement at room temperature was performed at 500 mbar, 750 mbar, and 900 mbar. The goal was to check the performance of the pulse stretched laser during rovibrational measurements under a variety of circumstances.

This is the only section where measurements were performed with a spectrograph grating of 1200 grooves/mm, as this was done in the early stages of applying the pulse stretched laser for experiments. As such, a broader wavelength range was chosen for a more complete image of the spectrum obtained. The slit width was adjusted to 250 µm centered around the laser, and clean air was pumped in with a flow rate of 1.5 SLPM.

Table 5.1: SNR of Raman measurements of N_2 *at room temperature.*

Pressure	Single shot (dB)	10 Shots (dB)	1000 Shots (dB)
500 mbar	2.4×10^{-4}	6.3×10^{-3}	1.7
750 mbar	3.8×10^{-4}	7.8×10^{-3}	2.7
900 mbar	2.8×10^{-4}	9.5×10^{-3}	3.4

5.1.2 Results and Discussion

All the measurements are summarised in table 5.1, showing the SNR. Additionally, the single shot measurement at 900 mbar is presented in Fig. 5.1. It shows the measured data, the background data, and the combined plotted data binned from pixel 500 to 600 with a hampel filter applied. The 1000 shots measurement at 900 mbar is presented in Fig. 5.2 in the same way.

It can be seen that the single shot measurement does show some signs of the vibrational ground state. However it is very small, and only appears when the intensity scale is set to a small margin. This relatively small signal compared to the background signal clearly has an effect on the spectrum presented in Fig. 5.1c. The ground state is visible, but the SNR is too low to allow for any serious modelling. It can be seen that the SNR significantly increases with the amount of shots taken. Even without looking at the SNR this is clear from the raw data by comparing Fig. 5.1a with Fig. 5.2a.

Additionally, the SNR rises with elevated pressures. This is caused by the enlarged concentration of species leading to an improved Raman intensity. This pressure dependence is not as visible during the single shot measurements. Perhaps the SNR of a single shot measurement is too low to accurately find the SNR.

This leads to the conclusion that single shot Raman measurements with the current setup are technically possible, but by no means near feasible. The effectiveness of a single shot measurement could be enhanced by supplying more energy per laser pulse. This can be done by improving the energy transmission of the pulse stretcher in the ways presented in section 3.3. Additionally getting a more powerful laser would increase the signal, although this could lead to the necessity of an additional optical cavity for enhanced time stretching. Another way to increase signal intensity is by upgrading our reflective grating spectrograph to a transmission grating spectrograph as they have a better diffraction efficiency and signal throughput [77].

More practical in the short term this simply leads to the age old conclusion that more shots offer a better signal to noise ratio. In line with this conclusion any further experiments were performed with as many shots as possible.

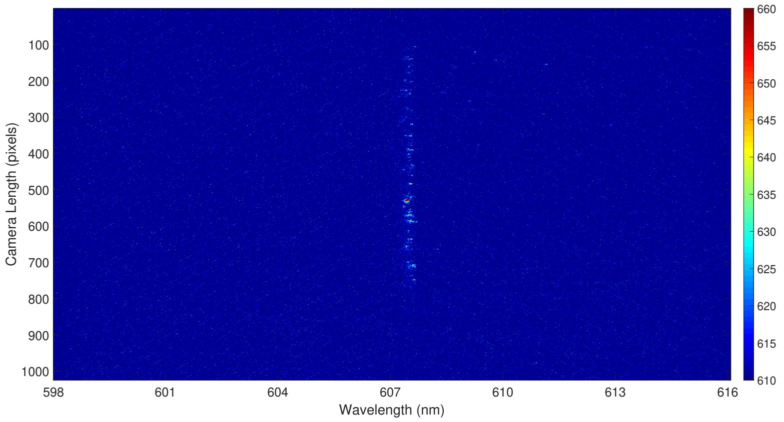

(a) *Raw data.*

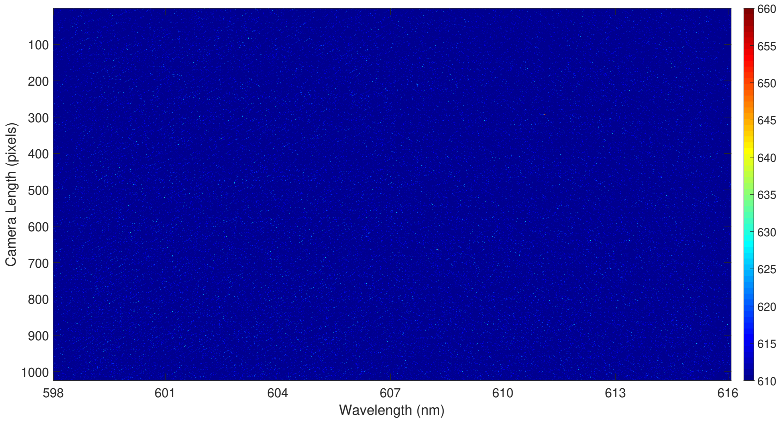

(b) *Background data.*

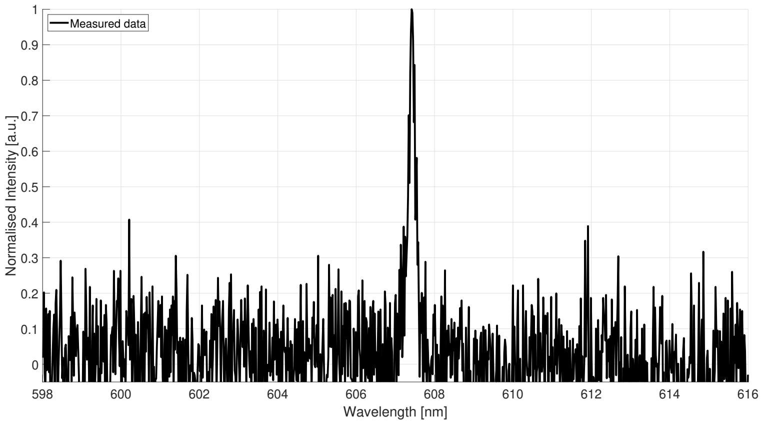

(c) *Plotted data binned from pixel 500 to 600, with Hampel filter.*

Figure 5.1. *Single laser shot Raman data of* N_2 *at 900 mbar.*

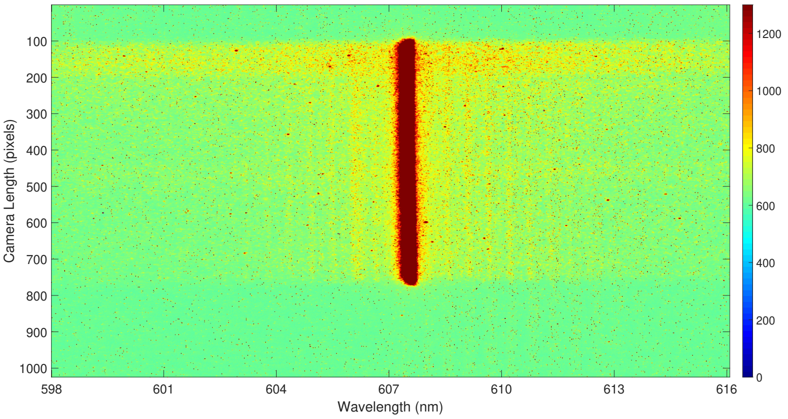

(a) *Raw data.*

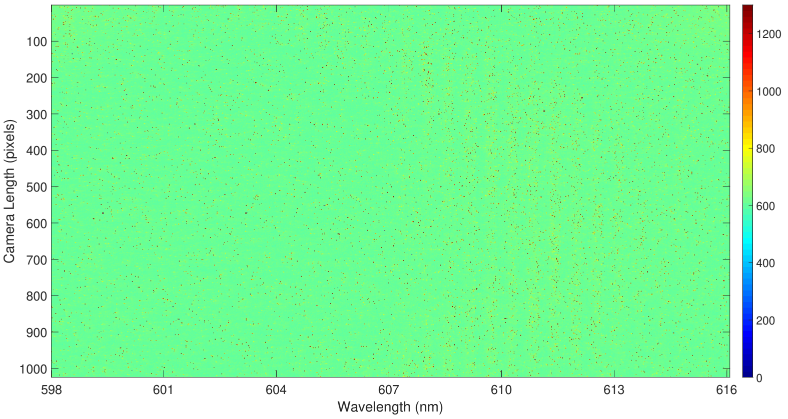

(b) *Background data.*

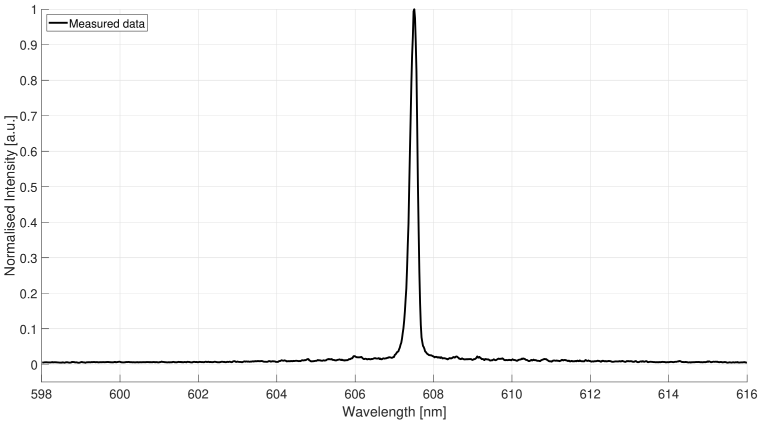

(c) *Plotted data binned from pixel 500 to 600, with Hampel filter.*

Figure 5.2. *Raman data of* N_2 *after 1000 laser pulses at 900 mbar.*

5.2 Post-Discharge Temperature (500 mbar)

It has been noted by Ravi Patel that the plasma streamers are able to ignite a flame after the first few plasma pulses. As such, the post-discharge temperature of N_2 has been researched to get an insight into the thermal developments. Additionally a measurement like this would allow for a comparison of rovibrational measurements with Lo *et al* (2012) [49], as a means to further test the use of the pulse stretched laser for Raman purposes.

5.2.1 Experiment Description

Preferably everything would be operated at atmospheric pressure (because most industrial application will take place there), however the plasma is barely able to ignite at 1 bar. Therefore these experiments were performed at 500 mbar which would lower the breakdown voltage according to the Paschen curve (Fig. 2.2). Specifically for the gap between the electrodes in Fig. 4.2 this would lead to a *pd* of 300 torr cm.

The compressed air was pumped in with a volumetric flow rate of 1.5 SLPM, which was also the approximate flow rate during combustion ignition. As such, plasma images were taken with the camera and spectrograph in imaging mode with the slit width fully open to check the stability of the plasma. It should be noted, however, that while flame ignition occurred at this flow rate of air; the flow channel during combustion was different from the one in this experiment. The combustion ignition took place in a quartz tube with a influx area of $0.16\,\mathrm{cm}^2$. Our measurements took place in the full volume of the vacuum vessel with an area perpendicular to the flow direction of $5 \times 10^2\,\mathrm{cm}^2$. As such the real flow rate will scale down accordingly.

For the Raman measurements the slit width was adjusted to 250 µm centered around the laser. The diagnostics laser was aimed through the air gap exactly between the electrodes (so perpendicular to the plasma streamer direction). This lead to another reason why operating at 500 mbar would be beneficial: the frequency of optical breakdown occurring nears 0.

Additionally, because the post-discharge temperature of the first few plasma pulses was to be researched, the pulse generator was set to operate in burst mode. This way the species had time to relax again in between measurement shots. This also had the benefit that the voltage generator would not overheat as quickly, leading to increased measurement times.

Specifically the pulse generator was set to produce 100 bursts (at 3 kHz). Preferably fewer bursts would be used to be able to better measure the initial plasma pulses, however at 500 mbar at least 100 bursts were necessary to sustain the plasma for the length of time required for measurements.

Subsequently the post-discharge temperature after the 70^{th} burst was measured instead of the 100^{th} burst to simulate being closer to that initial plasma pulse.

A total of 1800 shots were taken, which constitutes a total measurement time of 3 minutes with the 10 Hz laser. After this the high voltage generator was generally too overheated to sustain the plasma for any longer.

6 Post discharge delays were measured: 200 ns, 500 ns, 1 µs, 10 µs, 100 µs, and 200 µs.

5.2.2 Results and Discussion

To start of, the 1 µs post-discharge delay measurement was picked to sample the SNR. With the snr() function of MATLAB it has been determined that the SNR for this measurement was around 2.69 dB.

Looking at the cropped plasma images at two moments in time (Fig. 5.3) it can be seen that the plasma streamer is not very stable in regards to its position. This is most likely caused by the active flow rate of the air. The plasma seems most stable and strongest at the position of the ground electrode (to the left side of Fig. 5.3). However, for the Raman measurements the laser is aimed directly through the middle of the slit width at the 2.5 mm mark (so perpendicular to the plasma). At this position there is a clear perpendicular movement of the plasma streamer (in the order of $\Delta 2$ mm), which could potentially lead to a discrepancy in the data analysis.

Sadly, the laser could not be aimed closer to the ground electrode because the screw thread was not long enough to move the electrode higher. Additionally the Brewster window at the entry point of the laser also did not allow for any more directional freedom. However, for the temperature determination the data has been vertically binned from 10.3 mm to 12.6 mm, which would mean that movements such as in Fig. 5.3b would still be included in the data. However, this would only account for such movements in the direction exactly parallel to the laser, and not for movements perpendicular to the laser. Additionally, binning over such a large area guarantees the inclusion of non post-discharge molecules, which could bring down the average temperature.

The rovibrational temperature development that came forth from these measurements can be found in Fig. 5.4. It can be seen that the vibrational temperature is clearly higher than the rotational temperature, which is attributed to the faster relaxation of the latter.

Comparing the absolute values of the temperatures with literature: Lo *et al* (2012) [49] report on vibrational temperatures starting at $T_{vib} = 7000\,\text{K}$ 200 ns in the post-discharge, before steadily decaying to $T_{vib} = 2000\,\text{K}$ 100 µs in the post-discharge. Our vibrational temperatures are steadily in the order of 800 K to 900 K, nearly a full order of magnitude

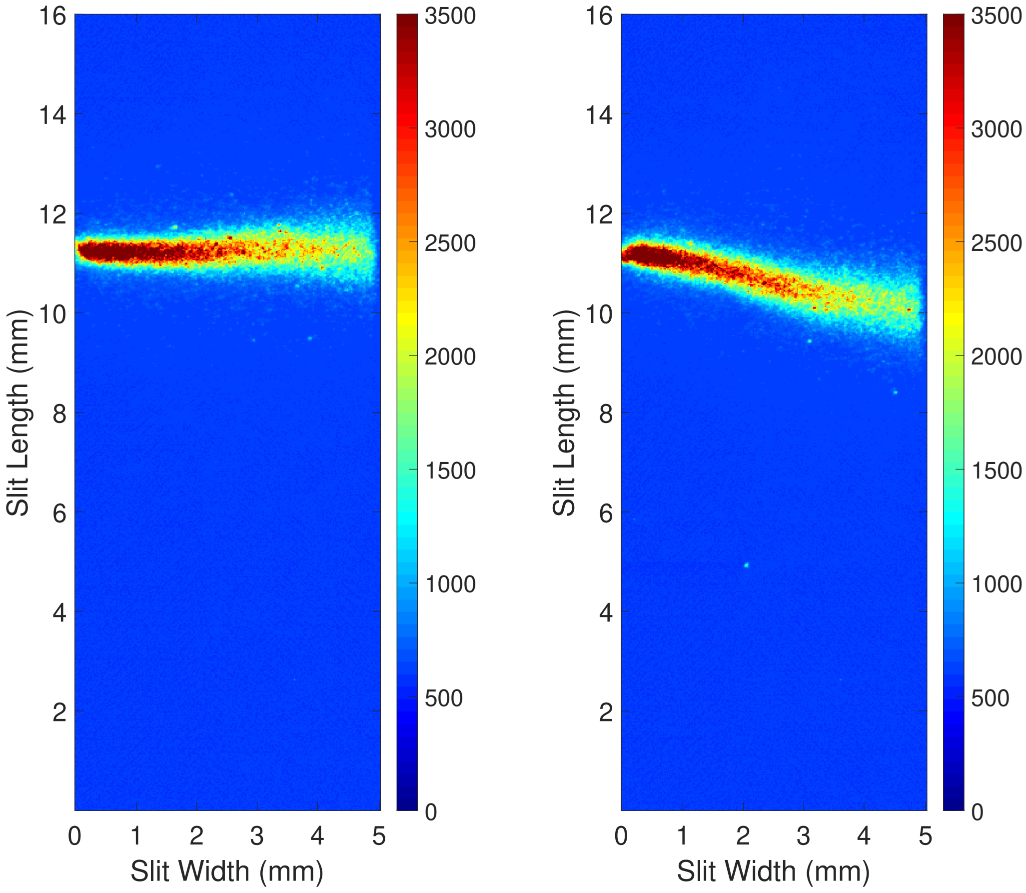

(a) *(b)*

Figure 5.3. *Example of plasma imaging (cropped) at two different times at 500 mbar under the experiment conditions. The colour scale is based on signal intensity.*

lower. Similarly their rotational temperatures range from $T_{rot} = 1000\,\mathrm{K}$ to 1500 K, compared to our 370 K to 410 K. Their higher temperature is especially noteworthy considering they operate at 525 torr cm, which would imply a harder time to energize electrons.

The reason for their higher temperatures could be their longer HV pulse width (25 ns FWHM) at a similar voltage (20 kV), and higher current (65 A). This results in a pulse energy deposition of 20 mJ, which is about 5 times higher than what has been measured for our voltage supply (Fig. 4.3). Lo *et al* (2012) [49] also do not have an active airflow, but operate in quiescent conditions. In our case the flow rate (however small) could lead to cooling of the air plasma. They also do not use a DBD configuration,

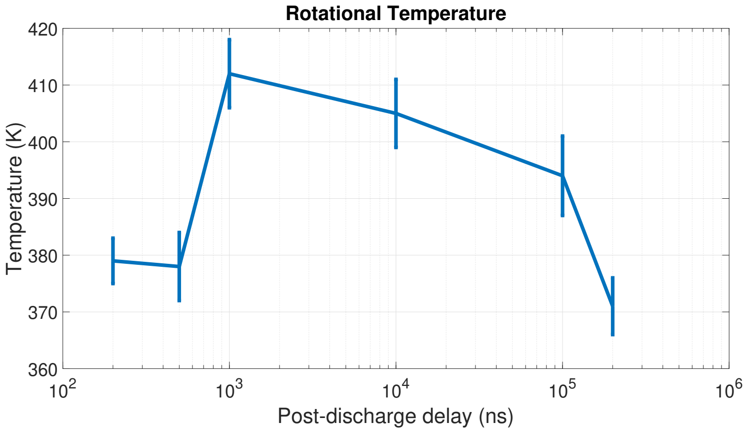

(a)

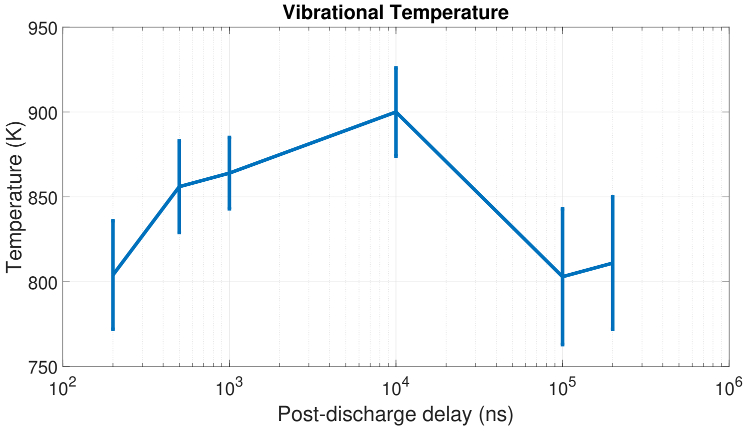

(b)

Figure 5.4. *Temperature development in the post discharge at 500 mbar.*

but simply have two copper electrodes in air. Our dielectric barrier could absorb a part of the HV pulse. Additionally DBDs often have a lower gas temperature due to the current inhibiting effect of the dielectric.

Another very likely reason for the lower temperature could be the plasma streamer moving outside of the focus spot of the laser due to the airflow, making for incomplete data acquisition. Other misalignment issues due to human operation error could also be to blame. If this has happened one would not be able to see it back in a worsened SNR: instead the signal would simply favour the ground vibrational band in a high resolution fashion. That being said, extra care has been taken to align the laser with the electrodes, so if laser misalignment is indeed the cause of this temperature it is most likely caused by the flow rate. As mentioned earlier, a lower temperature could be caused by the data being binned over too great an area compared to the size of the plasma, resulting in more non-discharged air to be included in the data analysis leading to a lower average temperature.

The rotational temperature development over an increasing post discharge delay does not seem to behave according to a clear pattern. In the case of the rotational temperature this is attributed to the fast relaxation which means it could reach a stable state before the first sample is taken. Lo *et al* (2012) [49] have conducted a similar experiment where the rotational temperature exhibits a near constant value during a post-discharge time-lapse, also attributed to fast relaxation. In our case the rotational temperature's lack of a pattern could be interpreted as simply a stable temperature hovering around a single value with some unaccounted for uncertainty.

The vibrational temperature was hypothesized to decrease during the post-discharge time-lapse, based on the results of Lo *et al* (2012) [49]. However, our measurement do not seem to showcase such a pattern, and in fact there is a hint of increasing temperature. Perhaps due to the low temperature measured in our case the relative differences over the time-lapse become too small to distinguish properly. Another reason for the lack of decay could be that we are creating some kind of steady state with our burst setting. The fast succession of voltage bursts could lead to some memory effects that allow for a continuous source of conduction in the air gap. Pai et al (2010) [78] have reported on creating a steady state plasma with nanosecond pulsed discharges. However, they continuously operate at 30 kHz and their steady state only occurs after 250 bursts: well beyond our burst regime. Additionally if we did have a steady state plasma we should be able to see plasma emission in the raw data, which we do not see.

It is worth noting that in the case of this experiment we are unable to measure beyond a 200 µs post discharge delay, due to the 3 kHz succession of bursts. Around 300 µs the next pulse starts to become visible, and as such we are no longer operating merely in the range of the previous pulse. Therefore, it was not possible to further research decay effects over a longer period.

Relating the measured vibrational temperature to the ignition temperature of stoichiometric methane-air mixtures at atmospheric pressure (870 K [79]), it is within the same realm. As such, combustion ignition with these streamers is not impossible, perhaps lending credibility to the idea that the measured temperature is in the correct ballpark. This comparison is based on the assumption that the vibrational temperature during the plasma is higher than what it is in the post-discharge.

Last but not least a temperature profile over space is plotted in Fig. 5.5 to explore the temperature development outside of the location of the plasma. This has only been done for the measurement with a 1 µs post-discharge delay. A temperature decay moving away from the plasma location is clearly visible, all the way down to room temperature for the rotational temperature. This does confirm the hypothesis that the higher vibrational bands we are seeing at the location of the plasma, are indeed lingering effects of said plasma in the post-discharge (seeing as they disappear at non-plasma locations). The vibrational temperature has increased uncertainty moving to either sides, which is attributed to the model desperately interpreting noise as very subtle vibrational bands. However, seeing as its just noise, this detection of 'vibrational' bands goes hand in hand with a high uncertainty.

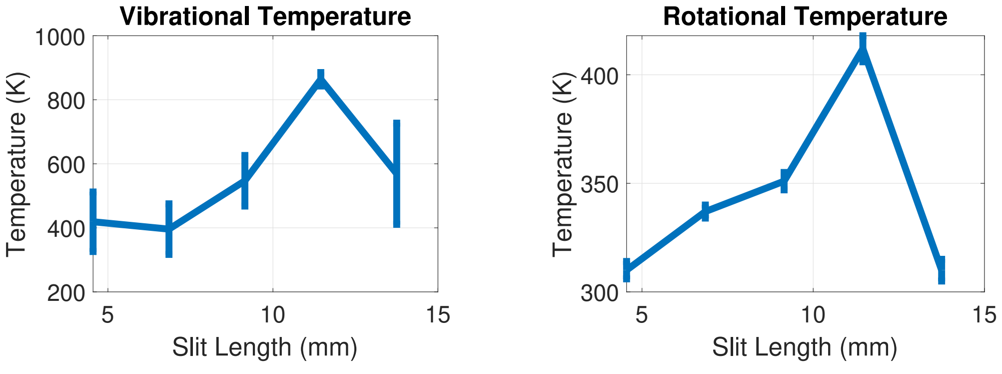

(a) *(b)*

Figure 5.5. *Rotational and vibrational temperature gradient in space (perpendicular to the plasma) at a* 1 µs *post discharge delay at 500* mbar*.*

5.3 Post-Discharge Temperature (100 mbar)

To increase measurement time a similar measurement was performed as in section 5.2, however this time at 100 mbar. This leads to a *pd* of 60 torr cm, which is only about 1 order of magnitude higher than the minimum breakdown voltage in the Paschen curve of N_2, leading to a more stable plasma.

5.3.1 Experiment Description

At this pressure the plasma could be sustained with only 3 bursts instead of 100 (at 3 kHz). At this burst setting the high voltage supply could operate continuously for at least a full afternoon. As such, every single measurement was performed at 18000 shots (30 minutes). This way a potentially better average signal could be gathered. A longer measurement time at 100 mbar compared to 500 mbar was also necessary because the Raman intensity decreases with pressure.

At 3 bursts it was also possible to better check the post discharge temperature of the initial bursts, rather than at the 70^{th} burst.

Once again the spectrograph slit width was opened to 250 µm centered around the laser, and again 6 post discharge delays were measured: 200 ns, 500 ns, 1 µs, 10 µs, 100 µs, and 200 µs.

Last but not least the flow rate of the compressed air was reduced to merely 0.15 SLPM. This should lead to a more stable plasma streamer, which was checked by taking camera images of the plasma similar to the previous section. At 500 mbar the experiments took place at 1.5 SLPM in an attempt to at least somewhat simulate a similar flowrate as during combustion. However, as mentioned in section 5.2.1, the actual flow rate during these plasma measurements differs due to the changed flow channel. As such the concept of trying to simulate the exact flow conditions during combustion ignition was abandoned, and this experiment is mostly focused on the post-discharge plasma characteristics.

5.3.2 Results and Discussion

Similar to the 500 mbar measurements, the 1 µs post-discharge delay measurement was picked to sample the SNR. With the snr() function of MATLAB it has been determined that the SNR for this measurement was around 5.63 dB. This is higher than the SNR during the 500 mbar measurements, which is attributed to the 10 times longer measurement time.

By observing the plasma imaging (Fig. 5.6) it was seen that the reduced flow rate lead to a more stable plasma. Even when multiple images were taken, the streamer continuously stayed at the same position. It can be also seen that the plasma is more diffuse than at 500 mbar. This could be caused by the lower breakdown voltage that is necessary at 100 mbar, leading to a greater area of ionization. The near-absent flow could potentially also lead to increased memory effects in the discharge gap leading to increased energies.

In regards to the modelled temperatures (Fig. 5.7 it can be seen that the rotational temperature (Fig. 5.7a) is still in the same ballpark as it was at 500 mbar (370-400 K). The vibrational temperature, however, seems to be about 200 K higher (Fig. 5.7b).

The higher temperature could be caused by the lower pressure which, as mentioned, gives rise to a faster induced breakdown as per the Paschen curve. The higher temperature could also be because of the significantly reduced airflow, thereby eliminating a potential cooling effect. The elimination of the air flow also leads to a better alignment of the diagnostics laser with the plasma streamer, meaning the averaged signal could now lean more towards a post-discharge temperature.

However, despite all the aforementioned reasons there is still no clear vibrational temperature decay, and in fact Fig. 5.7b seems to imply a rising vibrational temperature during the post-discharge time-lapse. In general

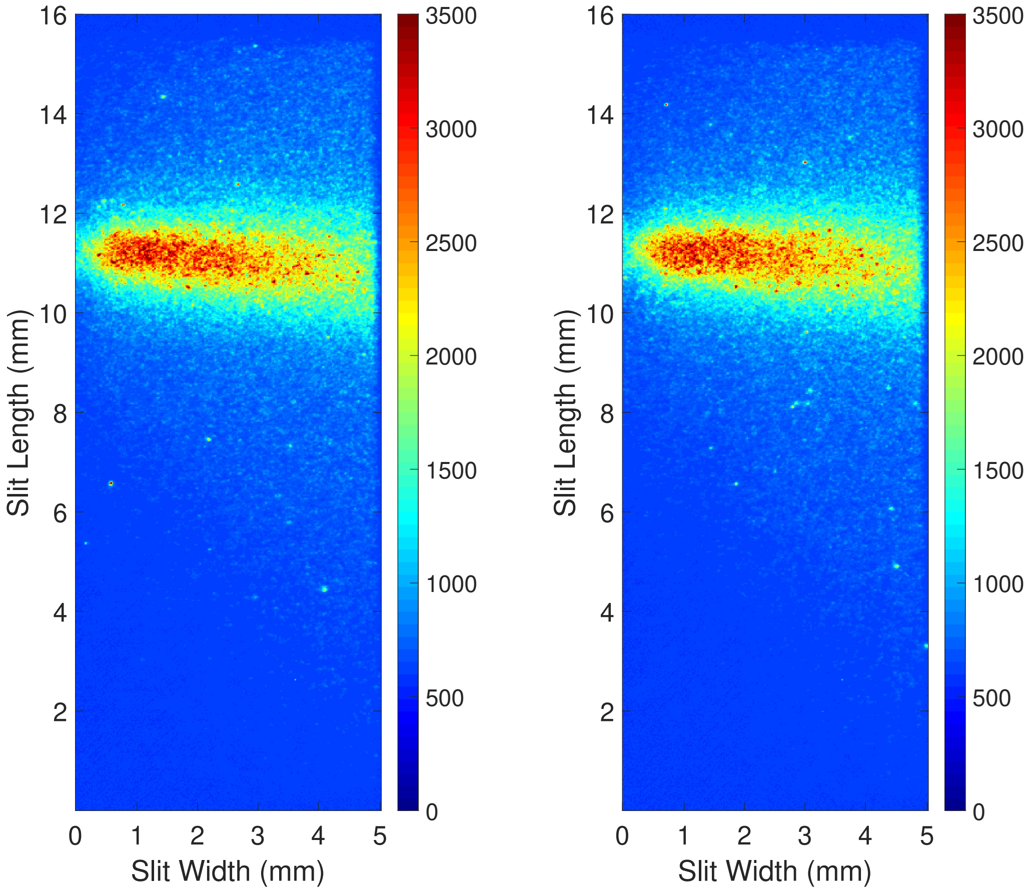

(a) *(b)*

Figure 5.6. *Example of plasma imaging at two different times at 100 mbar under the experiment conditions. The colour scale is based on signal intensity.*

all the proposed reasons for this in section 5.2.2 hold here as well, with the exception of the misalignment caused by an air flow. There could, however, still be a misalignment due to human operation error.

Once again the temperature gradient in space has been determined around the plasma at 1 µs post-discharge delay (Fig. 5.8). Here, too, it can be seen that the temperature is clearly higher at the position of the plasma, and decays as it moves away from it. What is interesting here, though, is that the temperature decay for T_{rot} is less steep than during the same measurement at 500 mbar. This can be attributed to the more diffuse plasma, which will increase the temperatures over a greater area. T_{vib} is harder to compare in this sense due to the high uncertainties when moving

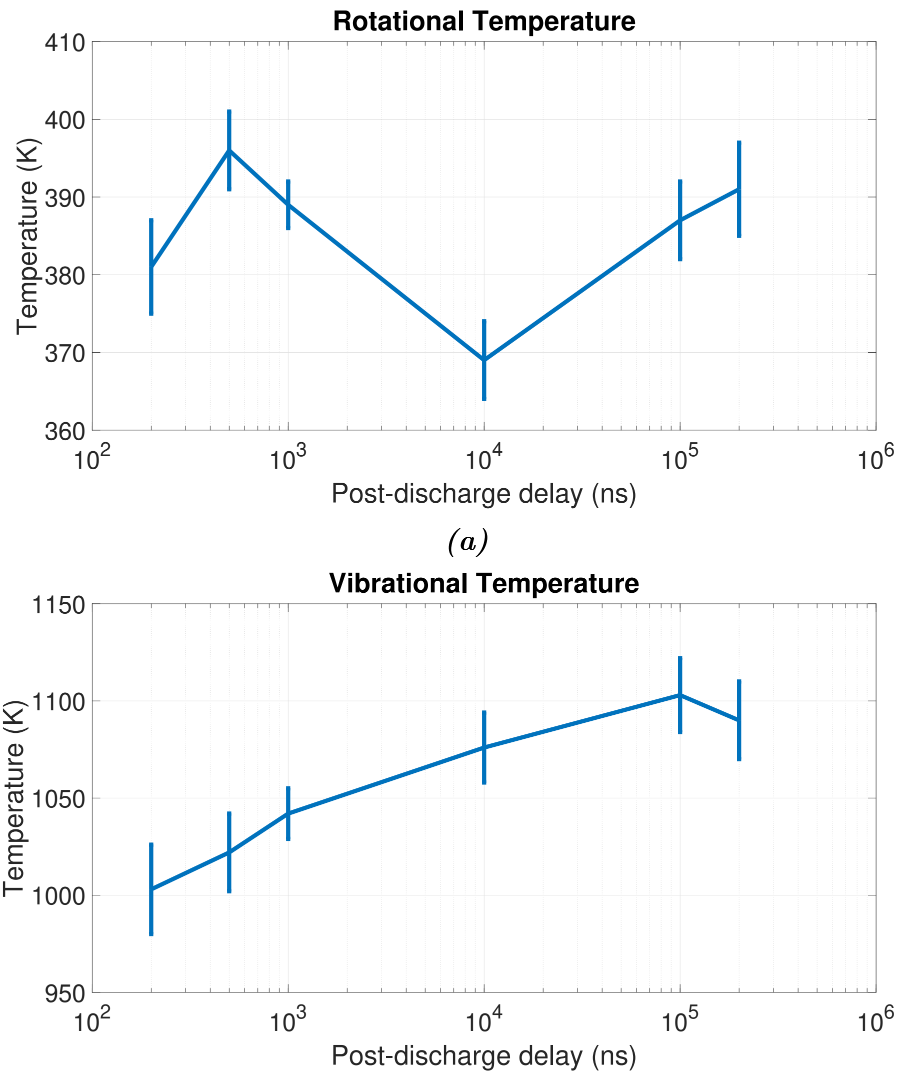

(a)

(b)

Figure 5.7. *Temperature development in the post discharge at 100 mbar.*

away from the post-discharge location.

At the end of the day it is difficult to draw any other conclusions from this data due to the single delay sweep that has been done per pressure value. Aside from the pressure difference between this experiment and the experiment in section 5.2, there was also the change in air flow rate, and amount of bursts produced by the HV electrode. These vastly different parameters make for a difficult comparison between these two experiments without leaning too far into speculation.

In the future it can be recommended to repeat the experiments without any parameters changed, before moving on to a new experiment where one only changes a single parameter. However, for the purposes of this thesis

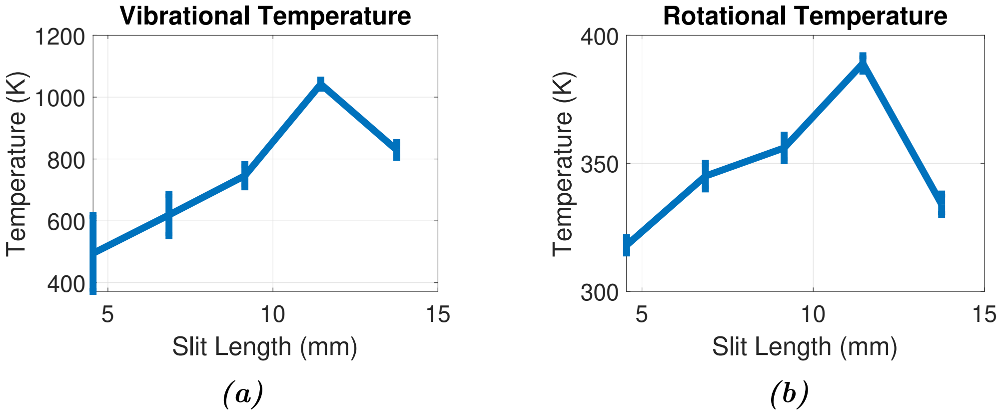

(a) ***(b)***

Figure 5.8. *Rotational and vibrational temperature gradient in space (perpendicular to the plasma) at a* 1 µs *post discharge delay at 100 mbar.*

the time in the lab was determined to be at an end, seeing as it could be concluded that the pulse stretcher did work as intended in observing higher vibrational bands.

This page is intentionally left blank

CHAPTER 6

Conclusions and Outlook

6.1 Conclusions

In conclusion it can be said that the pulse stretching setup that was build (consisting of a system of two optical cavities) was successful in stretching the Nd:YAG laser pulse out into a longer period of time. The original pulse width of the laser pulse was in the order of 9 ns, and after the pulse stretcher it was increased to around 40 ns.

The energy transmission of this system was not as successful as theoretically possible: only around 54% of the original laser pulse energy came out on the other end, versus the theoretical maximum of 87.0%. The result was a $(380 \pm 5)\,\mathrm{mJ}$ pulse. This was partially caused by an increased beam diameter and divergence resulting from the use of a telescope. This telescope was necessary because without it the uneven beam profile would damage optics. Additionally most of the optics used were 1 inch in diameter, which quickly became too small for the laser beam diameter. Lastly, the alignment has been done by hand which is very prone to slight errors leading to permanent energy losses after a certain amount of iterations within an optical cavity.

Compared to the previous laser that was used, this meant an increase in power from $P_{pulse,old} = 0.12\,\mathrm{MW}$ to $P_{pulse,new} = (9.5 \pm 0.1)\,\mathrm{MW}$, meaning an increase of almost 80 times. While this should definitely lead to an increased signal to noise ratio, it will not necessarily lead to faster measurements due to the previous laser having a faster repetition rate of 3 kHz versus the current 10 Hz.

Additionally it was shown that the stretched Nd:YAG laser no longer induced optical breakdown when focused in air at pressures below 500 mbar. Between 500 mbar and atmospheric pressure the optical breakdown frequency was reduced to less than once per minute. This was the main purpose of the pulse stretcher as it allows for the laser to be used for spontaneous Raman spectroscopy purposes.

The signal to noise ratio for a single shot measurement was not deemed good enough for any proper diagnostics purposes. While there was definitely a vibrational band visible with only one shot, it was too low in comparison with the background noise to be properly analysed. For actual viable measurements the experiments had to include more shots.

Measurements with more shots were performed in the post-discharge regime of a nanosecond pulsed DBD in air at two different pressures. It was found that there are indeed visible higher vibrational bands in the post-discharge, but they were almost a full order of magnitude lower than the expected value based on literature. They also did not behave according to the hypothesized pattern as the post-discharge delay increased.

At 500 mbar the vibrational temperature was in the order of 800-900 K, and the rotational temperature 370-410 K. At 100 mbar the vibrational temperature ranged from 1000-1100 K and the rotational temperature from 370-400 K. Literature values are in the order of 7000 K for vibrational temperatures, and 1000 K for rotational temperature. This discrepancy is most likely caused by a 5 times lower plasma pulse energy (4 mJ versus 20 mJ), the use of a dielectric, and potentially due to a misalignment of the diagnostics laser with the plasma pulse. The temperature difference between both pressures could be attributed to the differing flow conditions of the air present, and the difference in breakdown voltage according to Paschen's law.

At both pressures the temperature development over an increasing post-discharge delay (ranging from 200 ns to 200 µs) seems relatively stable for the rotational temperature, which is attributed to the fast relaxation of the rotational temperature even before measurements start. However, the vibrational temperature was hypothesized to decay over the measured time-lapse, but this does not clearly occur. Potentially a steady state is created with the continuous operation of the plasma in a burst setting, or perhaps laser-plasma misalignments are to blame here as well.

6.2 Outlook

Further improvements of the pulse stretcher could be to fix the laser profile which could then result in eliminating the telescope from the setup. This should lead to a smaller and less diverging laser beam resulting in a better energy transmission. Additionally one could increase the sizes of the mirrors used, allowing for more energy to be captured (and thus transmitted) within the cavities. More extreme improvements could consist of introducing motor driven mirror mounts for the optical cavities, actively governed with the help of CCD cameras.

With the current state of the pulse stretched laser Raman spectra are observed after a single laser shot. However, it does not have a high enough SNR to be used for actual experiments. To increase the signal one could consider upgrading the spectrograph to a transmission grating spectrograph (versus the reflective grating currently in use) for less signal loss. One could also consider upgrading to a more powerful laser, but this could potentially lead to the necessity of more optical cavity to reduce the peak power further. Additionally other labs have reported on using 4 pulse stretched lasers firing consecutively to get a clear Raman signal within 500 ns. There was also a problem with the laser-camera synchronisation leading to the necessity of gate width of 125 ns. If this synchronisation were to be fixed, the gate width could be operated closer to the 40 ns of the laser.

To improve the post-discharge measurements one could try looking more into alignment of the laser with the plasma. It would also help to repeat experiments more often under the same conditions to make sure that the measured signal is indeed what is physically happening.

This page is intentionally left blank

Bibliography

[1] S. Chu and A. Majumdar, "Opportunities and challenges for a sustainable energy future," *Nature*, vol. 488, no. 7411, pp. 294–303, 2012.

[2] A. Kumar, K. Kumar, N. Kaushik, S. Sharma, and S. Mishra, "Renewable energy in India: Current status and future potentials," *Renewable and Sustainable Energy Reviews*, vol. 14, no. 8, pp. 2434–2442, 2010.

[3] N. Oreskes, "E SSAY on Climate Change," *Science*, vol. 306, no. January, pp. 2004–2005, 2005.

[4] E. Byers and ET AL, "Global exposure and vulnerability to multi-sector development and climate change hotspots," *Environmental Research Letters*, vol. 13, no. 5, 2018.

[5] Environmental Protection Agency (EPA), "Nitrogen oxides (NOx), why and how they are controlled," *Epa-456/F-99-006R*, no. November, p. 48, 1999.

[6] S. Pathmanathan, M. T. Krishna, A. Blomberg, R. Helleday, F. J. Kelly, T. Sandström, S. T. Holgate, S. J. Wilson, and A. J. Frew, "Repeated daily exposure to 2 ppm nitrogen dioxide upregulates the expression of IL-5, IL-10, IL-13, and ICAM-1 in the bronchial epithelium of healthy human airways," *Occupational and Environmental Medicine*, vol. 60, no. 11, pp. 892–896, 2003.

[7] M. W. Frampton, J. Boscia, N. J. Roberts, M. Azadniv, A. Torres, C. O. Christopher, P. E. Morrow, J. Nichols, D. Chalupa, L. M. Frasier, F. Raymond Gibb, D. M. Speers, Y. Tsai, and M. J. Utell, "Nitrogen dioxide exposure: Effects on airway and blood cells," *American Journal of Physiology - Lung Cellular and Molecular Physiology*, vol. 282, no. 1 26-1, pp. 155–165, 2002.

[8] M. Nicholas, D. Hall, and N. Lutsey, "Quantifying the electric vehicle charging infrastructure gap across U.S. markets," no. January, 2019.

[9] A. W. Schäfer, S. R. H. Barrett, K. Doyme, L. M. Dray, A. R. Gnadt, R. Self, A. O'Sullivan, A. P. Synodinos, and A. J. Torija, "Technological, economic and environmental prospects of all-electric aircraft," *Nature Energy*, vol. 4, no. 2, pp. 160–166, 2019.

[10] ICAO, "Electric, Hybrid, and Hydrogen Aircraft-State of Play," no. September 2015, pp. 124–130, 2016.

[11] Y. Ju and W. Sun, "Plasma assisted combustion: Dynamics and chemistry," *Progress in Energy and Combustion Science*, vol. 48, no. C, pp. 21–83, 2015.

[12] A. Starikovskiy and N. Aleksandrov, "Plasma-assisted ignition and combustion," *Progress in Energy and Combustion Science*, vol. 39, no. 1, pp. 61–110, 2013.

[13] A. Elkholy, *Development of Non-thermal DBD Microplasma Reactor for Combustion Applications.* PhD thesis, Eindhoven University of Technology, 2019.

[14] G. Cléon, D. Stepowski, and A. Cessou, "Long-cavity Nd:YAG laser used in single-shot spontaneous Raman scattering measurements," tech. rep., 2007.

[15] F. Fuest, *1D Raman/Rayleigh-scattering and CO-LIF measurements in laminar and turbulent jet flames of dimethyl ether using a hybrid data reduction strategy.* PhD thesis, Technischen Universität Darmstadt, 2011.

[16] M. Lieberman and A. Lichtenberg, "Principles of Plasma Discharges and Materials Processing: Second Edition," *Principles of Plasma Discharges and Materials Processing, 2nd Edition, by Michael A. Lieberman, Alan J. Lichtenberg, pp. 800. ISBN 0-471-72001-1. Wiley-VCH , September 2003.*, vol. 30, 9 2003.

[17] Krishnavedala, "Paschen curves," *Wikipedia, https://en.wikipedia.org/wiki/File:Paschen_curves.svg*, 2014.

[18] Nehra, Dwivedi, and Ashok, "Atmospheric Non-Thermal Plasma Sources," *International Journal of Engineering*, vol. 2, pp. 53–68, 2008.

[19] D. U. Pal, M. Kumar, H. Khatun, and A. Sharma, "Discharge characteristics of dielectric barrier discharge (DBD) based VUV/UV sources," *Journal of Physics: Conference Series*, vol. 114, p. 012065, 5 2008.

[20] R. Brandenburg, “Corrigendum: Dielectric barrier discharges: progress on plasma sources and on the understanding of regimes and single filaments (Plasma Sources Science and Technology (2017) 26 (053001) DOI: 10.1088/1361-6595/aa6426),” 7 2018.

[21] D. Rusterholtz, “Nanosecond Repetitively Pulsed Discharges in Atmospheric Pressure Air,” 12 2012.

[22] S. R. Turns, *An Introduction to Combustion: Concepts and Applications*. New York: McGraw-Hill, third ed., 2012.

[23] F. Xing, A. Kumar, Y. Huang, S. Chan, C. Ruan, S. Gu, and X. Fan, “Flameless combustion with liquid fuel: A review focusing on fundamentals and gas turbine application,” 2017.

[24] A. A. Perpignan, A. Gangoli Rao, and D. J. Roekaerts, “Flameless combustion and its potential towards gas turbines,” 2018.

[25] J. G. Wünning, “Flameless combustion and its applications,” *Proceedings of GTI Natural Gas Technologies 2005: What s New and What s Next*, pp. 1–12, 2005.

[26] A. Mze Ahmed, S. Mancarella, P. Desgroux, L. Gasnot, J. F. Pauwels, and A. El Bakali, “Experimental and numerical study on rich methane/hydrogen/air laminar premixed flames at atmospheric pressure: Effect of hydrogen addition to fuel on soot gaseous precursors,” in *International Journal of Hydrogen Energy*, vol. 41, pp. 6929–6942, Elsevier Ltd, 5 2016.

[27] S. Liu, T. L. Chan, Z. He, Y. Lu, X. Jiang, and F. Wei, “Soot formation and evolution characteristics in premixed methane/ethylene-oxygen-argon burner-stabilized stagnation flames,” *Fuel*, 2019.

[28] L. P. Yang, E. Z. Song, S. L. Ding, R. J. Brown, N. Marwan, and X. Z. Ma, “Analysis of the dynamic characteristics of combustion instabilities in a pre-mixed lean-burn natural gas engine,” *Applied Energy*, 2016.

[29] S. L. Ding, E. Z. Song, L. P. Yang, G. Litak, C. Yao, and X. Z. Ma, “Investigation on nonlinear dynamic characteristics of combustion instability in the lean-burn premixed natural gas engine,” *Chaos, Solitons and Fractals*, 2016.

[30] H. Zhou and C. Tao, “Effects of annular N2/O2 and CO2/O2 jets on combustion instabilities and NOx emissions in lean-premixed methane flames,” *Fuel*, 2019.

[31] J. O'Connor, S. Hemchandra, and T. Lieuwen, "Combustion instabilities in lean premixed systems," in *Lean Combustion: Technology and Control: Second Edition*, 2016.

[32] M. Jadidi, S. Moghtadernejad, and A. Dolatabadi, "A Comprehensive Review on Fluid Dynamics and Transport of Suspension/Liquid Droplets and Particles in High-Velocity Oxygen-Fuel (HVOF) Thermal Spray," *Coatings Journal*, vol. 5, pp. 576–645, 10 2015.

[33] I. A. Zlochower, "Experimental flammability limits and associated theoretical flame temperatures as a tool for predicting the temperature dependence of these limits," *Journal of loss prevention in the process industries*, vol. 25, pp. 555–560, 5 2012.

[34] W. T. Brande, "The Bakerian Lecture: On Some New Electro-Chemical Phenomena.," *Proceedings of the Royal Society of London*, vol. 1, no. 0, pp. 480–481, 1814.

[35] T. 'Denton, *Development of the automobile electrical system.* revised ed. ed., 2013.

[36] A. Starikovskiy and N. Aleksandrov, "Plasma-assisted ignition and combustion," 2 2013.

[37] A. Elkholy, Y. Shoshyn, S. Nijdam, J. A. van Oijen, E. M. van Veldhuizen, U. Ebert, and L. P. de Goey, "Burning velocity measurement of lean methane-air flames in a new nanosecond DBD microplasma burner platform," *Experimental Thermal and Fluid Science*, vol. 95, pp. 18–26, 7 2018.

[38] W. Sun, X. Gao, B. Wu, and T. Ombrello, "The effect of ozone addition on combustion: Kinetics and dynamics," *Progress in Energy and Combustion Science*, vol. 73, pp. 1–25, 7 2019.

[39] C. Cathey, J. Cain, H. Wang, M. A. Gundersen, C. Carter, and M. Ryan, "OH production by transient plasma and mechanism of flame ignition and propagation in quiescent methane-air mixtures," *Combustion and Flame*, vol. 154, pp. 715–727, 9 2008.

[40] S. Stepanyan, G. Vanhove, P. Desgroux, and S. Starikovskaia, "Time-resolved electric field measurements in nanosecond surface dielectric discharge. Comparison of different polarities. Ignition of combustible mixtures by surface discharge in a rapid compression machine.," in *51st AIAA Aerospace Sciences Meeting including the New Horizons Forum and Aerospace Exposition*, Aerospace Sciences Meetings, American Institute of Aeronautics and Astronautics, 1 2013.

[41] P. A. Caton, L. J. Hamilton, and J. S. Cowart, "Understanding Ignition Delay Effects With Pure Component Fuels in a Single-Cylinder Diesel Engine," *Journal of Engineering for Gas Turbines and Power*, vol. 133, 11 2010.

[42] N. B. Colthup, L. H. Daly, and S. E. Wiberley, "CHAPTER 1 - VIBRATIONAL AND ROTATIONAL SPECTRA," in *Introduction to Infrared and Raman Spectroscopy (Third Edition)* (N. B. Colthup, L. H. Daly, and S. E. Wiberley, eds.), pp. 1–73, San Diego: Academic Press, 1990.

[43] B. T. Sutcliffe, "The Born-Oppenheimer Approximation," in *Methods in Computational Molecular Physics* (S. Wilson and G. H. F. Diercksen, eds.), pp. 19–46, Boston, MA: Springer US, 1992.

[44] D. J. Griffiths, *Introduction to quantum mechanics.* Upper Saddle River, NJ: Pearson Prentice Hall, 2005.

[45] Mike Blaber, "19.3: The Molecular Interpretation of Entropy - Chemistry LibreTexts."

[46] S. S. Harilal, B. E. Brumfield, N. L. Lahaye, K. C. Hartig, and M. C. Phillips, "Optical spectroscopy of laser-produced plasmas for standoff isotopic analysis," *Applied Physics Reviews*, vol. 5, 6 2018.

[47] A. G. Brenton, "Translational-energy spectroscopy: a personal perspective of its development," *International Journal of Mass Spectrometry*, vol. 200, no. 1, pp. 403–422, 2000.

[48] J. Zhu, A. Ehn, J. Gao, C. Kong, M. Aldén, M. Salewski, F. Leipold, Y. Kusano, and Z. Li, "Translational, rotational, vibrational and electron temperatures of a gliding arc discharge," *Optics Express*, vol. 25, p. 20243, 8 2017.

[49] A. Lo, G. Cléon, P. Vervisch, and A. Cessou, "Spontaneous Raman scattering: A useful tool for investigating the afterglow of nanosecond scale discharges in air," *Applied Physics B: Lasers and Optics*, vol. 107, no. 1, pp. 229–242, 2012.

[50] P. J. Bruggeman, N. Sadeghi, D. C. Schram, and V. Linss, "Gas temperature determination from rotational lines in non-equilibrium plasmas: A review," 2014.

[51] O. Cardona and M. G. Corona-Galindo, "Calculation of the maximun number of vibrational and rotational energy states for diatomic molecules," tech. rep., 2012.

[52] L. Komorowski and P. Ordon, "Vibrational softening of diatomic molecules," *Theoretical Chemistry Accounts: Theory, Computation, and Modeling (Theoretica Chimica Acta)*, vol. 105, pp. 338–344, 4 2001.

[53] Moxfyre, "Energy-level diagram showing the states involved in Raman spectra.," *Wikipedia, https://en.wikipedia.org/wiki/Raman_spectroscopy#/media/File:Raman_energy_levels.svg*, 2009.

[54] D. C. Harris and M. D. Bertolucci, *Symmetry and spectroscopy : an introduction to vibrational and electronic spectroscopy.* Dover Publications, 1989.

[55] R. R. Jones, D. C. Hooper, L. Zhang, D. Wolverson, and V. K. Valev, "Raman Techniques: Fundamentals and Frontiers," *Nanoscale research letters*, vol. 14, p. 231, 7 2019.

[56] C. Hessels, "Quantitative analysis of non-premixed flames using Raman spectroscopy," tech. rep., Eindhoven University of Technology, 2017.

[57] J. Pelders, "Rovibrational temperature determination of the plasma and the methane flame in a nanosecond DBD microplasma burner using spontaneous Raman spectroscopy," tech. rep., Eindhoven University of Technology, 2019.

[58] A. V. Sepman, V. V. Toro, A. V. Mokhov, and H. B. Levinsky, "Determination of temperature and concentrations of main components in flames by fitting measured Raman spectra," *Applied Physics B: Lasers and Optics*, vol. 112, pp. 35–47, 8 2013.

[59] Spectra-Physics, "Quanta-Ray® Nd:YAG Laser Family," pp. 1–5, 2014.

[60] Photonics-Industries-International, "DM-527 Series DM Nd:YLF System Specifications," 2013.

[61] Y. P. Raizer, *Gas discharge physics.* Berlin : Springer, 1991.

[62] T. X. Phuoc, "Laser spark ignition: Experimental determination of laser-induced breakdown thresholds of combustion gases," *Optics Communications*, vol. 175, no. 4, pp. 419–423, 2000.

[63] J. Kojima and Q.-V. Nguyen, "Laser pulse-stretching with multiple optical ring cavities," *Applied Optics*, vol. 41, no. 30, p. 6360, 2002.

[64] D. Geyer, *1D-Raman / Rayleigh Experiments in a Turbulent Opposed-Jet.* PhD thesis, Technischen Universität Darmstadt, 2004.

[65] K. Hoffmeister, *Development and Application of High-Speed Raman/Rayleigh Scattering in Turbulent Nonpremixed Flames.* PhD thesis, Ohio State University, 2015.

[66] Thorlabs, "DET025A(/M) Free Space Window Input Si Biased Detector User Guide," tech. rep., 2017.

[67] LeCroy, "WaveRunner ® Xi-A Series Performance Reimagined 400 MHz to 2 GHz Performance Reimagined 400 MHz to 2 GHz," tech. rep., 2009.

[68] Kashiyama, "NeoDry NeoDry Series," tech. rep., 2012.

[69] Pfeiffer, "RVC 300, Control unit gas regulating valves," tech. rep.

[70] Megaimpulse, "NPG-18_3500,"

[71] EdmundOptics, "TECHSPEC_Filters_2017-1_EN_web,"

[72] Acton, "SpectraPro-500i 0.500 Meter Focal Length Triple Grating Imaging Monochromator / Spectrograph Acton Research Corporation SpectraPro-500i Operating Instructions," tech. rep.

[73] PrincetonInstruments, "PIMAX 3 - 1024i,"

[74] P. Instruments and d. of Roper Scientific, "WinSpec/32 Software User's Manual," tech. rep., 2012.

[75] Rigol, "DG1000Z Series Function/Arbitrary Waveform Generator," tech. rep.

[76] R. K. Pearson, Y. Neuvo, J. Astola, and M. Gabbouj, "Generalized Hampel Filters," *EURASIP Journal on Advances in Signal Processing*, vol. 2016, no. 1, p. 87, 2016.

[77] IbsenPhotonics, "The benefits of transmission grating based spectroscopy," tech. rep., 2010.

[78] D. Z. Pai, D. A. Lacoste, and C. O. Laux, "Nanosecond repetitively pulsed discharges in air at atmospheric pressure—the spark regime," *Plasma Sources Science and Technology*, vol. 19, no. 6, p. 065015, 2010.

[79] J. U. Steinle and E. U. Franck, "High Pressure Combustion – Ignition Temperatures to 1000 bar," *Berichte der Bunsengesellschaft für physikalische Chemie*, vol. 99, pp. 66–73, 1 1995.

This page is intentionally left blank

APPENDIX A

Practical Guide to Building a Pulse Stretcher

In this appendix you will find a step-by-step guide on how best to build a pulse stretcher as described in chapter 3.2, when you do not have access to motorised equipment and CCD cameras. First carefully read through the preliminary comments in section A.1. After this you can move on to the steps described in section A.2.

I have composed this guide based on my own trial and error, and therefore personal preference on how to tackle the obstacles inherent in the system. If you find a certain part too cumbersome and know of a better way: feel free to deviate. However, if it is your first time working with a system like this I would not recommend to do things off the cuff too much.

A.1 Preliminary Comments

- **Most importantly**: Align the system on a per-cavity basis, starting at the first (longest) cavity. Do not switch to the second (or third) cavity before completing all steps to perfection for cavity one.

- Use a diaphragm. This simple tool will be your best friend throughout the entire journey.

- It is better (and in the long run: *faster* even,) to take a full day to complete a single step, than to rush through and have to start over again and again.

- Every step is just as important as the next: do *not* skip a step.

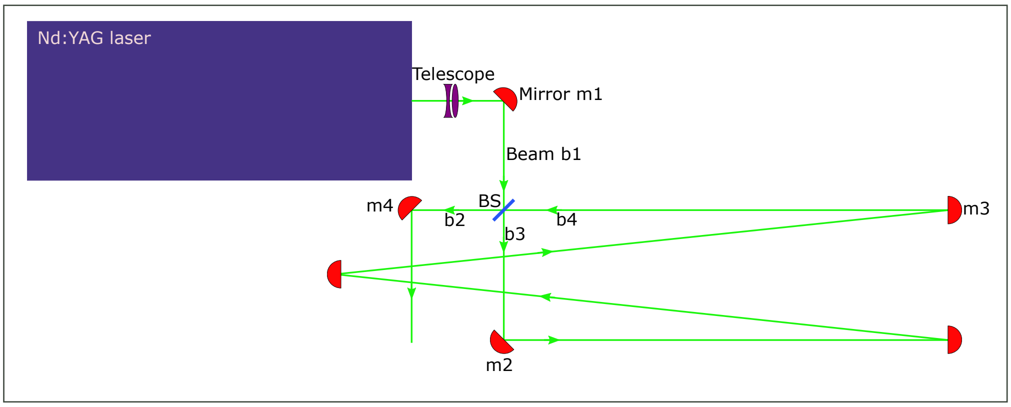

Figure A.1. *The general design of a single pulse stretcher cavity. Mirrors m_1 to m_4, beamparts b_1 to b_4, beamsplitter BS and the lens-configuration (Telescope) have been given special names for in-text references.*

- This guide is on how to do the *alignment* of the cavities. The technicalities in regards to specific optics are discussed in chapter 3.

- Operate the Nd:YAG laser with the Q-switch turned on for the best representation of the laserbeam as it will be when used for your eventual experiments. However, also make sure to operate at a low-energy setting to not damage yourself, or your colleagues. This low-energy setting is especially important at steps that use positive lenses such as step 9. Focusing a high energy laser will lead to breakdown (otherwise, what are you doing here reading this guide?), and will damage equipment and humans.

- Every time you add a new piece of optics, first make sure that its exact position is as good as possible before trying to 'fix' its orientation by fine tuning the kinetic knobs on the mount. After you have found the correct position and orientation on the table you can tightly screw it down, and it should barely need fine tuning.

- The important pieces of optics will be given a name as illustrated in figure A.1

- Do not forget to have fun, and remember: lasers are cool.

A.2 Step-By-Step Guide

1. As the laserbeam comes out of the telescope insert a mirror (m_1) to properly direct it onto the optical table at a 90° angle (45° angle of incidence).

2. Make note of the exact height of the beam as it is reflected off m_1. This height will henceforth be referred to as h_1. Measure this height as close to m_1 as possible to get the best idea of the vertical position of the beam.
3. Fix your diaphragm to h_1.
4. Check if you've done step 1 correctly: place the diaphragm in the far field to make sure the beam is still going in a straight line 90° relative to the original output of the laser. Adjust the knobs on m_1 for fine tuning while you keep going back and forth with the diaphragm.
5. Place the beamsplitter in your desired position on the optical table. Adjust its height so that the original beam (b_1) hits the beamsplitter in the middle. Adjust the orientation so that the reflected part of the beam (b_2) is as close to 90° as you can get it. You can check the far field beam position of the reflection with your diaphragm, but do not bother too much yet with fine tuning of the knobs on the beamsplitter. Fine tuning the beamsplitter only happens in step 9.
6. Place the first mirror of the cavity (m_2) at your desired position on the optical table. Adjust its height so that the part of the beam that got transmitted through the beamsplitter (b_3) hits m_2 in the middle. This height should be h_1, if it is not: make sure it is by going back to step 4.
7. Place all the other mirrors you need for your cavity to ensure the correct path length on the optical table in your desired locations. Make sure they are all at h_1 and fine tune the knobs of the mirrors so that they hit their next counterparts at this exact height as well.

   Liberally use your diaphragm to ensure the correct heights all through the cavity.
8. Take extra care when placing the last mirror of the cavity (m_3). m_3 Should always be oriented in a straight line aiming towards the beamsplitter, at a 90° angle with b_1. In fact, beam b_1, b_2, b_3, and b_4 should form a perfect 90°-90°-90°-90°-cross at this point.

   Tip: To perfect a cross-like orientation of m_1, m_2, m_3, and the beamsplitter it helps to look at their relative positions from a birds-eye view. Use a stool to get a better look at it.

   Additionally make sure that mirror m_3 aims beam b_4 onto the middle of the beamsplitter at height h_1.

   When I said in the prelimenary comments that every step is equally important I lied: this step is arguably the most crucial and worth spending at least an hour on.

9. It is only at this point you will start to fine tune the knobs on the beamsplitter.

   First look at the direction of your second iteration within your cavity and adjust the beamsplitter knobs so that this second iteration also ends up at your beamsplitter.

   Only after you have fixed this, look at the output of the beamsplitter (beam b_2), and ever so slightly fine tune the beamsplitter and mirror m_3 simultaneously to best align the different beams of every iteration. Be careful at this point because both m_3 and the beamsplitter are crucial parts of the cavity, and adjusting them by too much might misalign the cavity entirely.

   Tip: To help with this you can place a (temporary) positive lens in beam b_2, this focuses your beam which helps exposing the different orientations of the 'different' beams (of every cavity iteration) at the output of the beamsplitter. Make sure to remove the positive lens again after you are done with this step.

   Tip: When you cannot get the different beams at the beamsplitter output (b_2) to overlap in the x-direction, it could be that beam b_1, b_2, b_3, and b_4 are not a perfect cross resulting in a permanent misalignment of your cavity. Go back to step 8 to check the relevant mirrors, and potentially even step 4.

10. Now, place a mirror (m_4) at the desired position inside beam b_2 to redirect the now-stretched-pulse towards the second cavity. This time you do not have to fix m_4 necessarily at height h_1. Instead, just place it in such a way that most of the energy of beam b_2 hits this centre of m_4.

    Redirect this beam at a 90° angle towards the second cavity, in a similar way you have done with m_1 in step 1. Similarly, take note of the height of m_4, and finally re-adjust your diaphragm to this new height h_2. Theoretically h_2 and h_1 should be exactly the same, however realistically they will probably slightly differ.

11. Check the far-field orientation of mirror m_4 with the diaphragm and make sure the reflected beam stays at height h_2 and a 90° angle with beam b_2. Adjust the kinetic mount knobs for fine tuning to ensure this.

12. To align the second cavity go back to step 5 and repeat the steps all the way down to step 9 (except now with h_2 instead of h_1). If you wish to add a third cavity also repeat steps 10 to 12.

    Otherwise, you are done! Congratulations, you now have a time-stretched laser pulse.

This page is intentionally left blank

APPENDIX B

Abandoned Pulse Stretcher Designs

B.1 $R_{bs} = 50\%$

The first design of the pulse stretcher used two 1 inch beamsplitters with reflectivity $R_{bs} = 50\%$. At the time we were aware that $R_{bs} = 40\%$ would be better for the peak power reduction, however we did not yet know where we could find unpolarised beamsplitters with custom reflectivity. As such, we bought off-the-shelf beamsplitters from Newport Corporation, with the specification closest to our needs.

This was also in a time when we were not yet aware of the uneven energy deposition of Fig. 3.1. As such, after building this setup it was found that at high energies the equipment got damaged leading to us trying to build around that by applying the diameter-increasing lens configuration. This lead to the design in Fig. B.1. The cavity lengths of $L_1 = 6\,\mathrm{m}$ and $L_2 = 3\,\mathrm{m}$ were based on a presumed pulse width of 10 ns. This would lead to 25% peak power compared to the original pulse.

Power-time measurements (versus simulation) showed that the setup did work as intended in stretching the pulse (Fig. B.1c). However, the transmitted energy that was measured often did not exceed 40%. There were times when it would hit the order of 50%, but these were never stable, and sometimes dropped back to 35% for no apparent reason. This was thought to be caused by all the reasons stated in section 3.3.1, however in this case we also worked with 1 inch beamsplitters, which caused major clipping of the beam right at the gate of the optical cavities.

Focusing this stretched pulse in a cleaned atmospheric pressure vacuum chamber did sometimes result in breakdown. However, at lower pressures this decreased significantly. So despite the unpredictable energy transmission the effect of this design seemed successful.

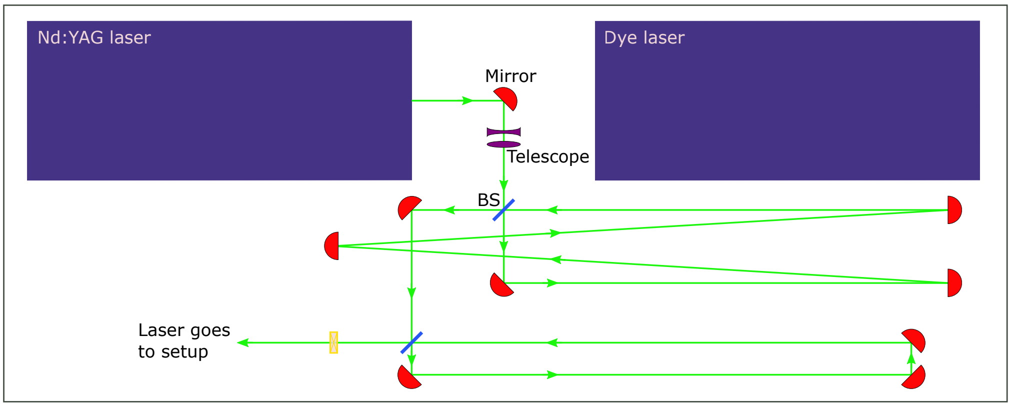

(a)

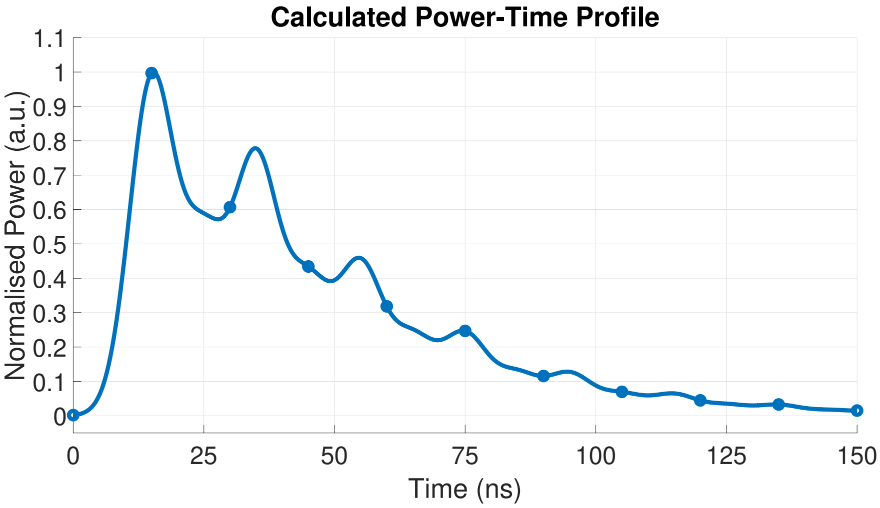

(b)

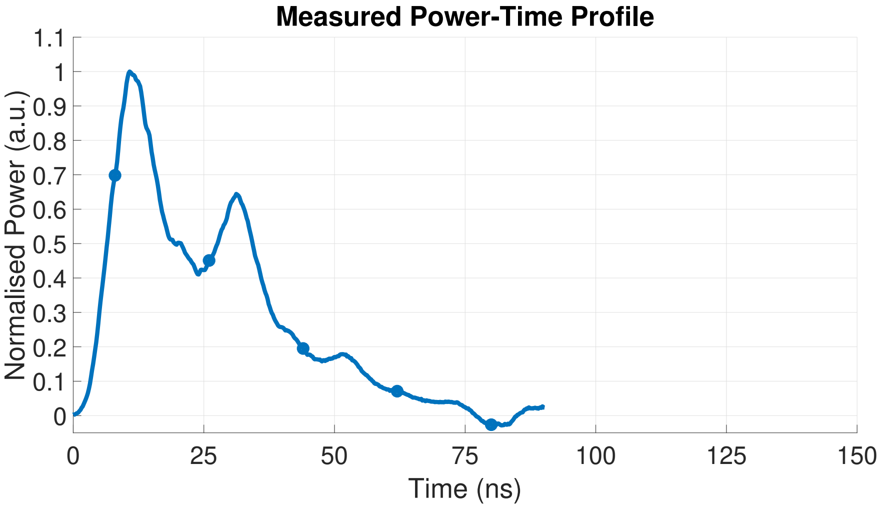

(c)

Figure B.1. *This configuration consists of two beamsplitters with reflectivity* $R_{bs} = 50\%$*, two cavities with pathlengths* $L_1 = 6\,\mathrm{m}$ *and* $L_2 = 3\,\mathrm{m}$*, and a half waveplate (HWP).*

However, at some point we figured out where we could obtain custom-made beamsplitters (Lattice Electro Optics), so it was decided to purchase replacements there. This way we could replace the damaged beamsplitters, and upgrade them to 2 inch $R_{bs} = 40\%$ beamsplitters in an attempt to improve the system.

B.2 $T_{bs,1} = 60\%$ and $R_{bs,2} = 40\%$

After we had received the two $R_{bs} = 40\%$ beamsplitters we took a step back and dove into the design process again. A configuration was developed where instead of using the reflectivity of both beamsplitters, instead we would use the *transmission* of one beamsplitter for the beampart going into the direction of the experimental setup (Fig. B.2). This would eliminate two mirrors from the setup as the cavities could be directly aligned (making alignment easier), and increase the amount of energy to be transmitted in the first few iterations (which were historically the best aligned iterations).

The drawback would be a relatively high peak power: 28% of the original pulse. However seeing as we only suffered minimally from optical breakdown with the previous design, we figured we could take the leap and try to push the boundaries of our peak power.

The energy transmission of this configuration turned out to be a huge success. With relative ease a 67% transmission was achieved. This was possible because a bigger part of the total energy was preserved within the first few iterations than with other designs we had tried. Additionally, because fewer mirrors were necessary there was an increase in retained energy, and we were also able to use some 2 inch mirrors at crucial locations.

The downside, however, was optical breakdown in the vacuum vessel. Even when going towards lower pressures the frequency of it happening was too high (multiple times per minute) to allow for measurements. The path length could be increased to reduce the peak power some more, but this would only lead to about 1 percent point lower peak power.

So eventually it was decided to go for two $R_{bs} = 40\%$ as described in section 3.2. Here the calculated laser peak power would be 22% of the original pulse, rather than the 28% of this design.

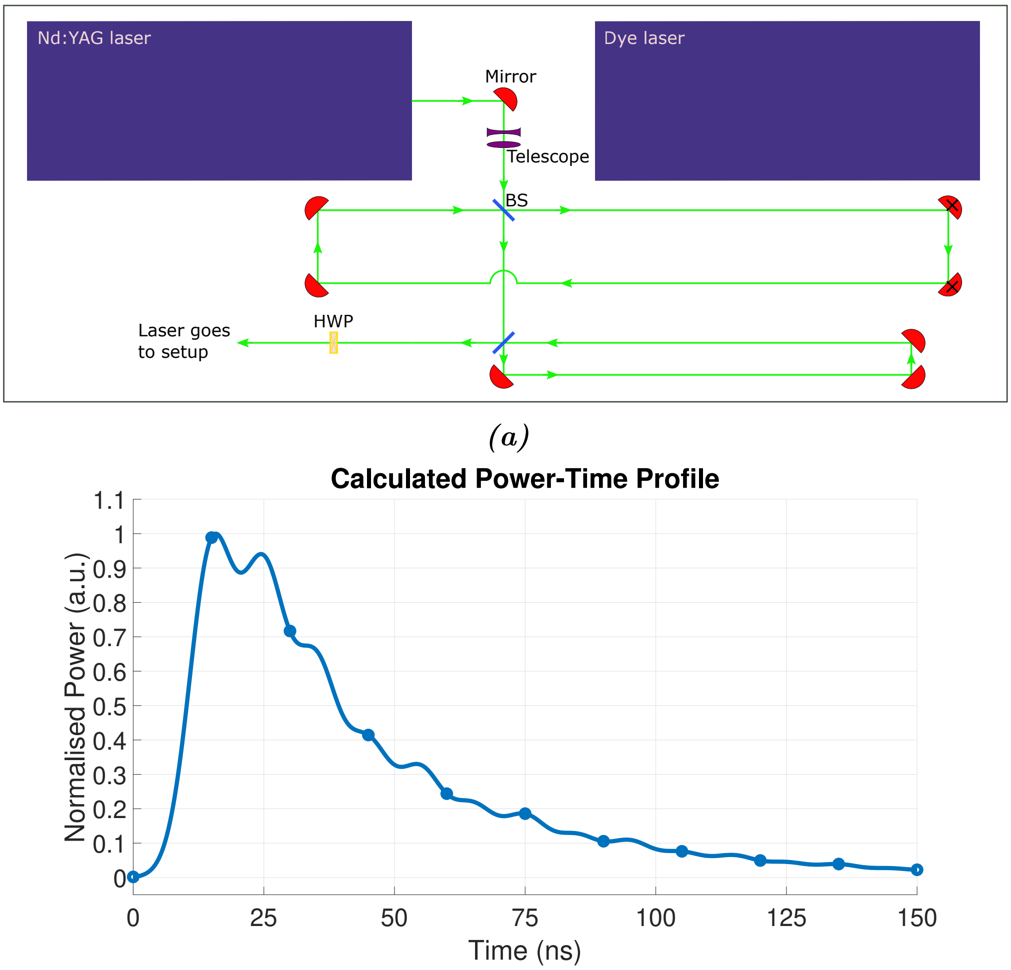

(a)

(b)

Figure B.2. *This configuration consists of a half waveplate (HWP), and two beamsplitters with reflectivity* $R_{bs} = 40\%$*, but with one configured with the transmission leading towards the setup. The two cavities have path-lengths* $L_1 = 4\,\mathrm{m}$ *and* $L_2 = 2.5\,\mathrm{m}$*. The mirrors with a cross are 2 inch in diameter, the others 1 inch.*

This page is intentionally left blank

APPENDIX C

Declaration of Scientific Code of Conduct

See next page.

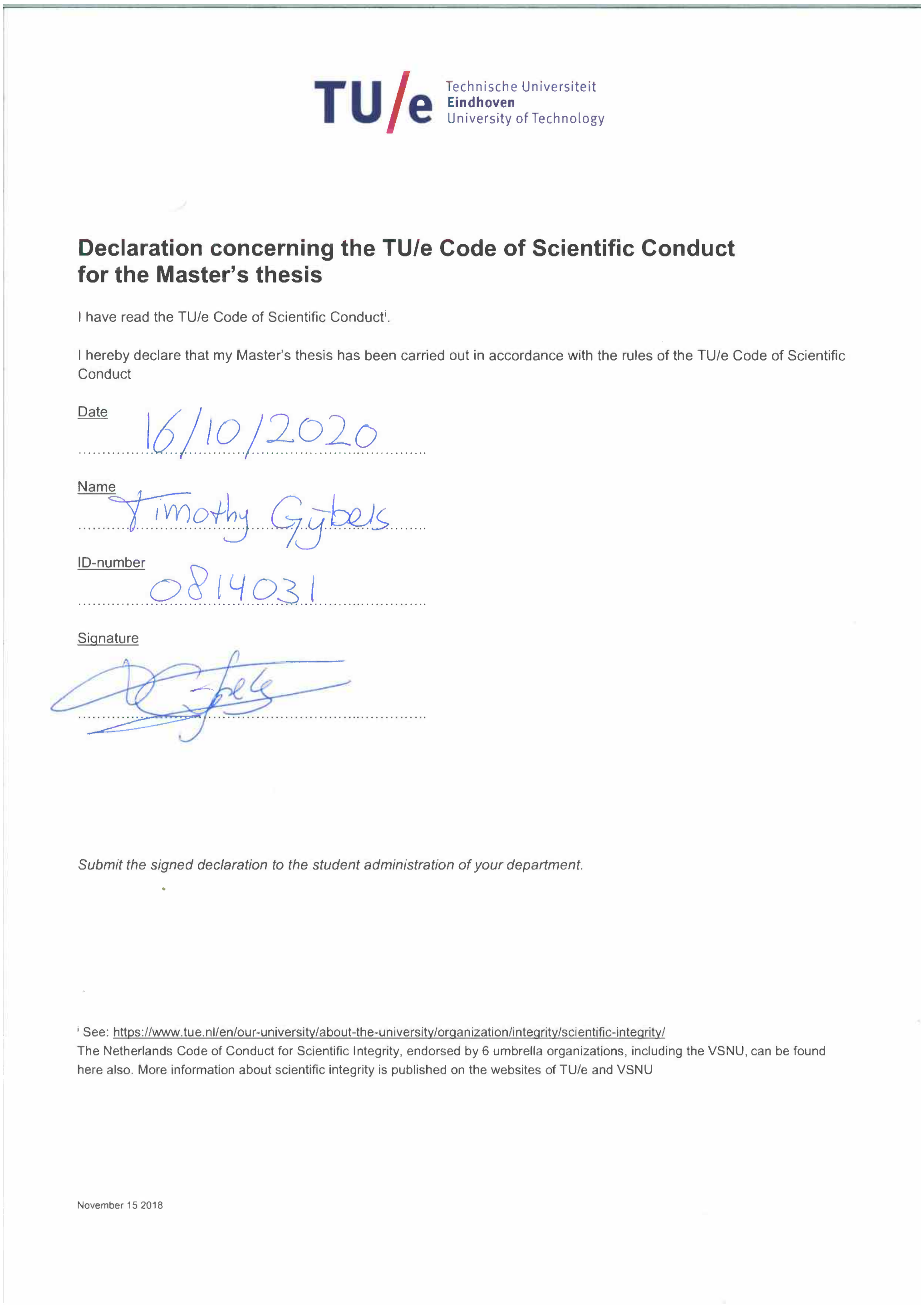

TU/e Technische Universiteit
Eindhoven
University of Technology

Declaration concerning the TU/e Code of Scientific Conduct for the Master's thesis

I have read the TU/e Code of Scientific Conduct[1].

I hereby declare that my Master's thesis has been carried out in accordance with the rules of the TU/e Code of Scientific Conduct

Date
16/10/2020

Name
Timothy Gybels

ID-number
0814031

Signature

Submit the signed declaration to the student administration of your department.

---

[1] See: https://www.tue.nl/en/our-university/about-the-university/organization/integrity/scientific-integrity/
The Netherlands Code of Conduct for Scientific Integrity, endorsed by 6 umbrella organizations, including the VSNU, can be found here also. More information about scientific integrity is published on the websites of TU/e and VSNU

November 15 2018

Figure C.1. *Declaration of TU/e Scientific Code of Conduct.*